Schisano, E, Rygl, KLJ, Molinari, S, Busquet, G, Elia, D, Pestalozzi, M, Polychroni, D, Billot, N, Carey, S, Paladini, R, Noriega-Crespo, A, Moore, TJT, Plume, R, Glover, SCO and Vazquez-Semadeni, E

The Identification of Filaments on Far-Infrared and Submillimiter Images: Morphology, Physical Conditions and Relation with Star Formation of Filamentary Structure

The Astrophysical Journal, 791:27 (23pp), 2014 August 10 doi:10.1088/0004-637X/791/1/27

THE IDENTIFICATION OF FILAMENTS ON FAR-INFRARED AND SUBMILLIMITER IMAGES: MORPHOLOGY, PHYSICAL CONDITIONS AND RELATION WITH STAR FORMATION OF FILAMENTARY STRUCTURE

E. Schisano[1,12], K. L. J. Rygl[2,12], S. Molinari[3], G. Busquet[4,12], D. Elia[3], M. Pestalozzi[3], D. Polychroni[5,12], N. Billot[6], S. Carey[1], R. Paladini[1], A. Noriega-Crespo[7], T. J. T. Moore[8], R. Plume[9], S. C. O. Glover[10], and E. Vázquez-Semadeni[11]
[1] Infrared Processing and Analysis Center, California Institute of Technology, Pasadena, CA 91125, USA; eugenio@ipac.caltech.edu
[2] European Space Research and Technology Centre (ESA-ESTEC), Keplerlaan 1, P.O. Box 299, 2200 AG Noordwijk, The Netherlands
[3] Istituto di Astrofisica e Planetologia Spaziali, INAF-IAPS, Via Fosso del Cavaliere 100, I-00133 Roma, Italy
[4] Instituto de Astrofísica de Andalucia, CSIC, Glorieta de la Astronomía, s/n, E-18008, Granada, Spain
[5] Departement of Astrophysics, Astronomy and Mechanics, Faculty of Physics, University of Athens, Panepistimiopolis, 15784 Zografos, Athens, Greece
[6] Instituto de RadioAstronomía Milimétrica Avenida Divina Pastora, 7, Núcleo Central, E-18012 Granada, Spain
[7] Space Telescope Science Institute, Baltimore, MD 21218, USA
[8] Astrophysics Research Institute, Liverpool John Moores University, 146 Brownlow Hill, Liverpool L3 5RF, UK
[9] Department of Physics and Astronomy and the Institute for Space Imaging Sciences, University of Calgary, Calgary, AB T2N IN4, Canada
[10] Zentrüm für Astronomie, Institut für Theoretische Astrophysik, Universität Heidelberg, Albert-Ueberle-Str. 2, D-69120 Heidelberg, Germany
[11] Centro de Radioastronomía y Astrofísica (CRyA), Universidad Nacional Autónoma de México, CP 58190 Morelia, Michoacán, Mexico
Received 2013 September 26; accepted 2014 June 16; published 2014 July 23

ABSTRACT

Observations of molecular clouds reveal a complex structure, with gas and dust often arranged in filamentary, rather than spherical geometries. The association of pre- and proto-stellar cores with the filaments suggests a direct link with the process of star formation. Any study of the properties of such filaments requires representative samples from different environments for an unbiased detection method. We developed such an approach using the Hessian matrix of a surface-brightness distribution to identify filaments and determine their physical and morphological properties. After testing the method on simulated, but realistic, filaments, we apply the algorithms to column-density maps computed from *Herschel* observations of the Galactic plane obtained by the Hi-GAL project. We identified ∼500 filaments, in the longitude range of $l = 216.^{\circ}5$ to $l = 225.^{\circ}5$, with lengths from ∼1 pc up to ∼30 pc and widths between 0.1 pc and 2.5 pc. Average column densities are between 10^{20} cm^{-2} and 10^{22} cm^{-2}. Filaments include the majority of dense material with $N_{\rm H_2} > 6 \times 10^{21}$ cm^{-2}. We find that the pre- and proto-stellar compact sources already identified in the same region are mostly associated with filaments. However, surface densities in excess of the expected critical values for high-mass star formation are only found on the filaments, indicating that these structures are necessary to channel material into the clumps. Furthermore, we analyze the gravitational stability of filaments and discuss their relationship with star formation.

Key words: ISM: clouds – ISM: structure – methods: data analysis – stars: formation

Online-only material: color figures

1. INTRODUCTION

Molecular clouds are the birthplaces of stars. Observations at different wavelengths and using different molecular tracers of the relatively best studied and nearby star-forming regions suggest complex morphologies, with the dust and gas arranged mostly along elongated, almost one-dimensional, filamentary structures (e.g., Hartmann 2002; Hatchell et al. 2005; Myers 2009). The *Herschel Space Observatory* (Pilbratt et al. 2010), thanks to its superior spatial resolution and sensitivity in the far-infrared, is now showing that the filamentary organization of the dense interstellar material is much more pervasive than was initially thought. From sub-parsec scales in nearby star-forming regions (André et al. 2010) to tens-of-parsecs scale along spiral arms (Molinari et al. 2010a), filaments appear to be key structures required to build the densities necessary for star formation. The abundance of compact star-forming seeds along these structures (see Elia et al. 2010; Henning et al. 2010), from pre-stellar to proto-stellar young condensations, indicates that filaments are where the initial conditions for star formation may be set.

Despite the ubiquity of filaments in star-forming regions, it is still unclear how they form and what their real relationship is with the mechanisms of star formation. Recent theoretical modeling of molecular cloud formation tends to produce filamentary structures formed by different mechanisms, like decaying supersonic turbulence (Padoan et al. 2007), cooling in the post-shock regions of large-scale colliding flows (Heitsch & Hartmann 2008; Vázquez-Semadeni et al. 2011), or global gravitational instabilities (Hartmann & Burkert 2007). While these predictions seem in qualitative agreement with observed morphologies, a detailed quantitative comparison has yet to be done. Significant advances are now possible with the availability of complete panoramic surveys of the Galactic plane, the Hi-GAL project (Molinari et al. 2010a), and nearby star-forming regions—like the Gould Belt project (André et al. 2010)—carried out with the *Herschel* satellite that, in principle, allow an unbiased characterization of filaments over a wide range of spatial scales and physical conditions.

Visual selection methods used in the recent past to identify the most obvious structures that appear elongated and the subsequent manual analyses to select portions of these filaments (e.g., Hartmann 2002; Hatchell et al. 2005; Busquet et al. 2013) become impractical when applied to large data sets. For example, the Hi-GAL project (whose data was used for this

[12] Also at Istituto di Astrofisica e Planetologia Spaziali, INAF-IAPS, Via Fosso del Cavaliere 100, I-00133 Roma, Italy.

work) mapped with *Herschel* for the entire Galactic plane at 70, 160, 250, 350, and 500 μm covering a total area of ∼720 square degrees (Molinari et al. 2010b). Filaments are found everywhere in Hi-GAL maps. Therefore, the quantitative and qualitative order-of-magnitude improvements in available data sets brought by *Herschel* require a change of perspectives when it comes to analysis methodologies. The problem of identifying specific patterns in images has already been faced by other scientific fields, particularly in computer engineering (see for example Gonzalez & Woods 2002), using ad hoc convolution with optimal filtering (like the Canny detector; Canny 1986) or studies of the local properties (topology) of the images (Hessian matrix studies, Skeleton, Morse Theory, and Shapefinders; Sheth et al. 2003). More related to astrophysics is the issue of determining the filamentary pattern from cosmological *N*-body simulations of the dark matter distributions (the cosmic web) or from the observed large-scale distribution of galaxies. To accomplish these goals, different approaches have been developed (see Aragón-Calvo et al. 2007 for a review) reaching different degrees of complexity.

More recently, Sousbie (2011) has presented a specific formalism (DisPerSE) based on the discrete Morse theory, which is able to recognize salient features of the large-scale cosmic web. The corresponding software has already been applied successfully to column density maps computed from the far-infrared/submillimeter data (e.g., Arzoumanian et al. 2011; Hill et al. 2011; Peretto et al. 2012). Nevertheless, the key issue for identifying particular patterns is defining the feature to be identified. Given a precise definition for the desired pattern, it is possible to determine the best method to highlight the defined structures. As an example, in the skeleton approach, as well as in DisPerSE, a filament is defined as the one-dimensional segment given by the central denser region of the extended elliptical structure. Thus, the skeleton is determined by choosing, from all the paths that connect the saddle points of the density (intensity) field to the local maxima, the one that, point by point, shows the smallest variation in the gradient (Novikov et al. 2006; Sousbie 2011). Such a definition allows the correct tracing of the ridge of the filaments.

In this paper, we consider filaments not as one-dimensional structures for which we simply trace the main ridge or spine, but instead as extended two-dimensional (2D) features that cover a portion of the map. Our aim is to identify the regions on the map that belong to the filamentary structure in order to derive its morphological and physical properties. To this end, we start by defining a filament as *an elongated region with a relatively higher brightness contrast with respect to its surrounding*, formalizing the intuitive idea of what a filament looks like based on what the eye sees on a map. Hence, instead of an approach involving the local extrema, we prefer to focus on a differential method, specifically the investigation of the eigenvalues of the Hessian matrix of the intensity (density) field, directly related to the contrast. Understanding where a filamentary structure merges into the surrounding background is the most critical point to be addressed because it not only determines the extent of the region, but also allows a realistic estimate of the background, without which a reliable determination of the properties of the filament is difficult to obtain.

We present here a method to detect and extract complex filamentary structures of variable intensity from 2D maps in the presence of high and variable backgrounds. In Section 2 we describe our methods, and in Section 3 we apply the algorithm to realistic simulations of filaments superimposed on real observed background fields, proving the strength and the reliability of the method to identify filaments. Finally, in Section 4 we apply the method to real data, extracting physical parameters of the filaments, and we list our main conclusions in Section 4.5.

2. IDENTIFYING FILAMENTS: THE METHODOLOGY

Differential methods have already been proven useful for highlighting structures like compact sources (e.g., the photometry code CuTEx (Molinari et al. 2011)) or filaments (see Figure 3 of Molinari et al. 2010a). In CuTEx the multidirectional second derivatives are used to enhance the portion of the map with the strongest curvature of the intensity field along four fixed directions (x, y, and the diagonals), corresponding to the compact source centers due to their particular symmetries. Molinari et al. (2011) have shown that the same operators qualitatively also trace the edges of extended structures like filaments. However, unlike sources, filaments are not strongly highlighted in the derivative along the four directions adopted by CuTEx. Therefore, we generalized the approach adopted with CuTEx by Molinari et al. (2011) to the specific case of filaments. To such aim, we initially follow the prescription described by Bond et al. (2010) for the classification of features (like filaments, voids, and walls) present in smoothed galaxy distributions. In their work, the authors noticed that each feature has a particular "fingerprint" of the curvature along the principal axis. For example, on first approximation, filaments can be considered as cylinder-like patterns that are more convex along one direction with respect to the orthogonal one; in particular, the difference in curvature between the two directions would be the highest if the chosen directions are along the cylinder axis (which would have a flat curvature) and the orthogonal radially directed one (which would have the larger convexity). As the curvature of an intensity map along any direction is proportional to its directional second derivative, the Hessian operator is most suited to characterize the spatial properties. Unlike the fixed directions adopted for CuTEx, the eigendecomposition of the Hessian matrix, $H(x, y)$, the emission intensity field $I(x,y)$ (dust thermal emission in the far-infrared in this particular case) immediately gives the directions of the principal axes at each position (x, y) of the observed map by means of the two eigenvectors, A_1 and A_2. The two eigenvalues λ_1 and λ_2 are proportional to the curvature at (x, y) along this direction. As we are focusing on the detection of emission features, we are interested in convex morphologies, that is $\lambda_1 \leqslant \lambda_2 \leqslant 0$. In this notation, we will assume that direction 1, being the one of maximum absolute curvature, will identify the cross-filament direction. A simple analysis of these eigenvalues can in principle give the direction, shape, and contrast of the local structure. For the case of a filament and near its axis, the relationship

$$\lambda_1 \ll \lambda_2 \leqslant 0 \quad (1)$$

should hold, with the filament axis defined by the direction of A_2. Although useful for tracing the features of simulations or relatively smooth data, this approach has some drawbacks when applied to maps of the interstellar medium. In fact, the above relation does not hold close to strong overdensities like, for example, compact clumps or cores found along the filament. In these cases, $\lambda_1 \simeq \lambda_2 \leqslant 0$ and therefore it is not possible to define the principal directions with enough accuracy. Moreover, Equation (1) only holds near the ridge of the filament, with the predominance of one eigenvalue with respect to the other weakening as one moves radially away

from the filament center. Although we have to relax the formal criteria in Equation (1) to identify filaments, maps of the second derivatives have the advantage that they filter out the large-scale emission and emphasize the more concentrated emission from compact sources and filaments (Molinari et al. 2010a, 2011). This is due to their ability to pinpoint strong variation in the gradient (i.e., change in the contrast) of the intensity distribution. Hence, whole filamentary regions, and not only their axis (hereafter "spine"), are included in the regions defined by a simple, conveniently chosen, thresholding of the second derivative map.

The pixel-to-pixel noise has a strong impact on the spatial regularity of the Hessian matrix, even for a relatively high signal-to-noise ratio map. In fact, the noise is amplified in the $H(x, y)$ by the derivative filter (i.e., by construction a high-frequency passband filter) and then it affects the estimation of the correct local eigenvalues λ_1 and λ_2. The amplitude of the increase of the noise depends on how the differentiation is implemented. For the case of a five-point derivative, see formula (3) of Molinari et al. (2011), we estimate an increase in the noise level of $\sim$20% on second derivative images and a further increase of $\sim$15% in the eigenvalue maps. Smoothing reduces the noise, but it also blurs the map, which damps the variations on the small spatial scales, and hence the contrast of the filament. Our tests indicate that smoothing through a Gaussian with HWHM of the order of an instrumental beam represents a reasonable compromise between the need for noise suppression and blurring of the structure. With such a choice the pixel-to-pixel noise is reduced roughly by a factor $\sim$two while the variation in the contrast decreases at the most by 20% with respect to the unsmoothed value.

Thus, for a given intensity map we then compute the Hessian matrix, and diagonalize and sort the eigenvalues in each pixel, producing two maps of eigenvalues $\lambda_1(x, y) \leqslant \lambda_2(x, y)$. We exclude from the analysis the pixels where $\lambda_1(x, y) \geqslant 0$, which identify concave shapes in the emission map. Two possibilities can occur for the remaining pixels: $\lambda_2(x, y) < 0$, which identifies convex regions, or $\lambda_2(x, y) \geqslant 0$ for saddle points. Both cases occur in typical filamentary features with modulated emission along the axis.

The next step is to threshold the eigenvalue map with the highest absolute value of λ_1 (x, y). The adopted threshold defines the lowest contrast that a region should exhibit to be considered as belonging to a filamentary structure. The optimal choice of the threshold depends on the condition of the map on which the user is working; in particular, it depends on the strength of the diffuse background emission and the pixel-to-pixel noise.

We apply a morphological closing operator with a structural element half as wide as the beam to smooth the edges of the identified regions on scales smaller than the beam, similar to what was done by Rosolowsky et al. (2010). Then, we proceed by identifying the connected regions of the thresholded image pixels and label them by progressive numbers; these regions are called regions of interest (RoIs). The border of each RoI represents a first rough estimate for the edges of the filament. However, since we use relaxed criteria with respect to Bond et al. (2010), different types of structures might contaminate the sample of candidate filaments. In particular, relatively roundish structures like large and elongated compact clumps, or clusters of compact objects lying on a strong intensity field, might also be selected. To remove this contamination we carry out an ellipse fit to each candidate RoI and discard all regions for which the axis ratio of the fitted ellipse is above a fiducial value of 0.75. Additionally, we also require the major axis to have a minimum length of three times the instrumental point-spread function (PSF) of the image, to exclude slightly elongated sources that cannot be considered as filaments. However, it is observed that there may be cases where filaments may intersect and generate a web-like structure that, depending on the contrast threshold adopted, may be cataloged as one single region; if the overall shape of the RoI happens to be more or less roundish, it would be discarded by the above criteria. To prevent this from happening we also compute the filling factor of the RoI as the ratio between the area of the RoI and the area of the fitted ellipse; regions whose filling factor is less than a fiducial value of 0.8 are kept as candidate filamentary structures. The fiducial ellipticity and filling factor threshold values adopted to identify and discard "roundish" clump structures have been determined from tests carried out on Hi-GAL maps; the values can, however, be modified as an input to the detection code.

Once the list of candidate filamentary RoIs has been decontaminated from compact roundish clumps or undersized elongated structures, we proceed to identify the spine of the filament by applying a morphological operator of "thinning" on each region (see Gonzalez & Woods 1992). In short, a "thinning" operator on a RoI works by correlating each pixel and its surrounding with specific binary masks defining specific patterns. These patterns are designed to determine if a pixel belongs to the RoI's boundary; in such a case the pixel is removed. We adopted a 3×3 binary mask, so the classification of a pixel as a boundary depends strictly on its closest neighbors. The same approach has already been applied in a different field, like the identification of filaments on the Sun (Qu et al. 2005). Under the assumption that the filament is symmetric in its profile, by repeating the procedure iteratively until no further pixels can be removed the surviving points constitute the spine of the filament. In the case of slightly elliptical blobs, the structure would reduce to few pixels, or even to one point in the circular case, that are filtered out when applying our criteria on minimum length. The spine pixels are then connected through a "minimum spanning tree", implemented with the Prim algorithm (Cormen et al. 2009), to define the unique path that joins them together. This allows us to identify nodal points where multiple branches depart and immediately enables the classification of structures in main hubs of peripheral branches. An example of the method applied over a very simple and bright simulated filament is given in Figure 1. The simulated filament has variable intensity along its spine with periodical fluctuation of amplitude equal to 20% and few compact sources of different size distributed along its axis; although this seems an idealized situation, the presence of the three sources would have caused the original method of Bond et al. (2010) to break the filament into three portions.

Our main goal in this exercise is to obtain the physical characterization of the filamentary structures. For example, we would be interested not only in knowing where filament spines are, but also what their masses are. To this aim, we also need to estimate the cross-spine size of the filament, as well as that of the underlying background level, which we need to subtract to obtain the true contribution to the emission of the filament material alone. To do so, for each spine point we fit the brightness profile in the direction orthogonal to the spine with a Gaussian function and compute the median of all the FWHM values obtained; an associated uncertainty is provided by the standard deviation of the individual width estimates along the filament (see Figure 2). A new region mask is then created, which is symmetrical around the spine and with total width

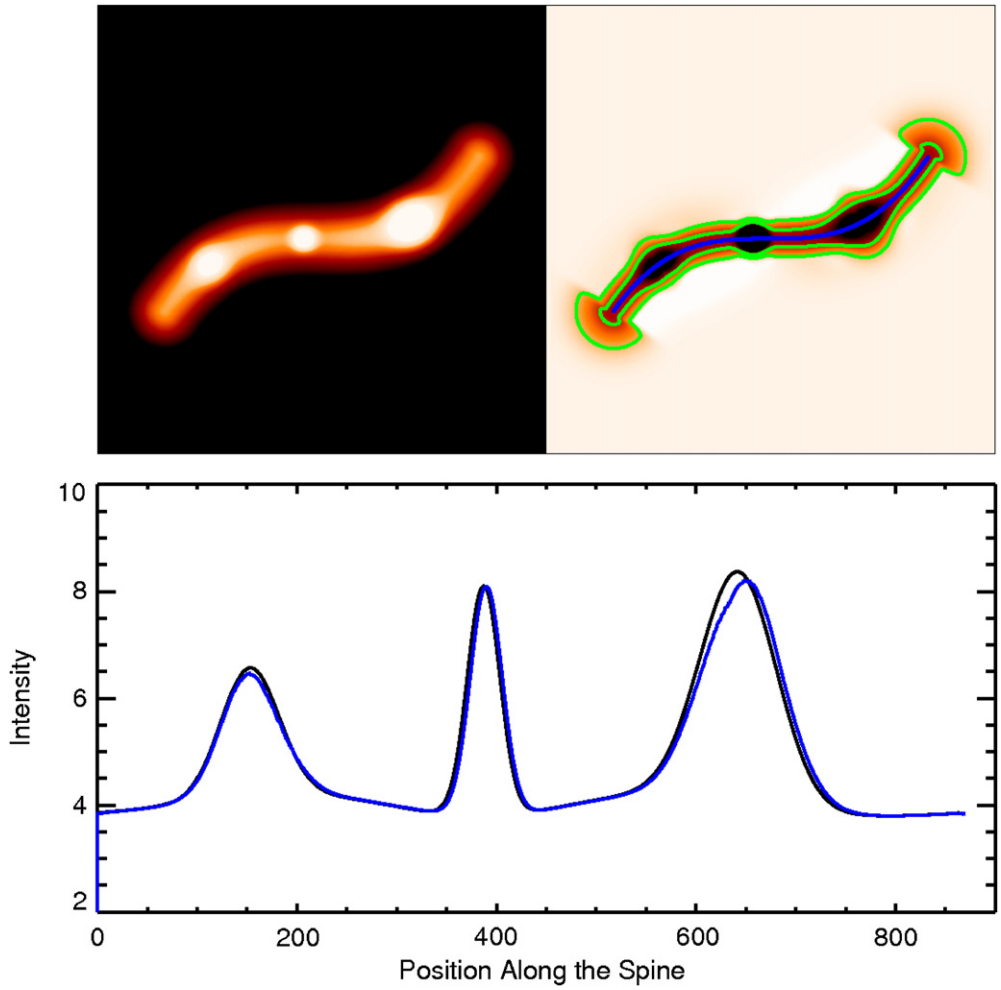

Figure 1. Example of our method applied to a single filament (top left panel) with a 20% flux modulation and three bright clumps distributed along its axis. The top right panel shows the image of the minimum eigenvalues of the Hessian matrix; the green contours mark the region of interest resulting from the thresholding at two different levels, a high and a low threshold, while the blue line represents the estimate of the spine of the filament after the "thinning" of the RoI. In the lower panel are shown the simulated filament spine profile (black) and the extracted profile for the low threshold (blue).

(A color version of this figure is available in the online journal.)

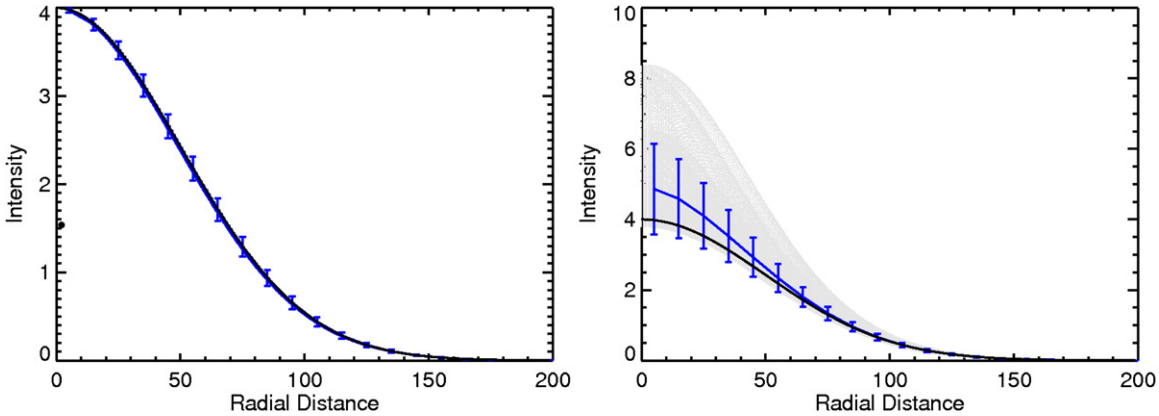

Figure 2. Example of the ability to retrieve the width of a simulated filament. In the left panel we see that the method retrieves (blue line) exactly the cross-spine width of the filament in input (black line) when the filament has no sources along its axis. In the right panel we show the results for the same filament in Figure 1; the ensemble of the cross-spine profiles (the set of gray points) shows more dispersion with respect to the width of the input filament (black line). The fit to these points (the blue line) represents the average filament cross-spine profile and it is overestimated with respect to the true value (although consistent within the uncertainty bars that reflect the spread of the filament width along the spine).

(A color version of this figure is available in the online journal.)

equal to twice the median filament FWHM. For very complex features where filaments are organized in web-like structures, the cross-spine profile fitting often fails to converge as there are not enough background pixels to reliably constrain the fit.

We then provide an additional measure of the filament width by adopting the initial RoIs identified by the Hessian eigenvalues thresholding, and enlarging them with the morphological "dilation" operator (Gonzalez & Woods 1992) applied three

times in sequence. The merit in doing this is that whatever the threshold adopted, the thresholding is always done over the map of minimum *but negative* eigenvalues; in other words, the pixels selected will always belong to regions where the curvature of the brightness profile in the maximum curvature direction is within the convexity region. This implies in general a conservative identification of the filament region, because it would neglect the wings of the filaments where the emission profile changes concavity before joining the background emission. In cases of isolated filaments where the cross-spine Gaussian fitting converges, we will show (see below) that the two width estimates are in very good agreement.

The measurement of the background level on which the filamentary structure is sitting is very important for a reliable measurement of the total emission of the filament, or of the total mass in case the filament detection is run on a column density map as we will show below. Once the filament RoI and spine have been determined, we proceed as follows. For each spine point we compute the direction perpendicular to the local spine, and select the pixels intersecting the two-pixels-wide boundary region surrounding the filament RoI on each side of the spine along such a direction. These two sets of pixels (one on each side of the filament) are fitted with a line producing a reliable local estimate for the background. This is repeated for all filament spine points, producing a detailed estimate of how the background varies along the filament.

3. CODE PERFORMANCES ON SIMULATED AND REAL FILAMENTS

To characterize the performance of the software in conditions that more closely resemble real situations, we carried out an extensive series of tests using sets of simulated filamentary structures superimposed on maps of the ISM emission showing a strongly variable background. As it is best to test in the most realistic conditions possible, we used maps from the Hi-GAL survey.

While the simplest and ideal shape of a filament is a homogeneous straight cylinder shape, those conditions are rarely (if ever) found in observations. Gravity, turbulence, and other evolutionary effects twist the orientation of the "ideal" shape and also gather the matter in different places along the original structure. Moreover, what we generally see is a 2D projection of a three-dimensional structure that, depending on the viewing angle, may significantly amplify any departure from the ideal elongated cylinder shape. A realistic filament is generated by first computing randomly twisted curves as the "spine" for the structure, with a variable profile along such curves up to 20% with respect to the mean intensity. The brightness distribution in the cross-spine direction is assumed to be Gaussian and in some cases we added compact sources of different sizes at different positions along the spine. Filaments were then randomly rotated to avoid any bias from specific orientations. Regridding of the simulation has been also included to estimate the effect of the pixelization on the performance of the method. We produced various sets of simulations, with different numbers of filaments and degrees of clustering, divided into two groups defined by the width of the structure simulated: unresolved, "thin," and resolved, "thick," filaments.

We want to stress here that our method is suited to identify extended, but still concentrated, emission. The emission from the large-scale structures is strongly dampened in the derivative maps, so broad filaments can only be detected if they have strong central intensities. In fact, the dampening in the derivative map increases with the spatial scales, following a power-law behavior with an exponent of two for scales $\geqslant$6 pixels (i.e., two times the PSF for Nyquist sampled maps; see also S. Molinari 2014, in preparation). Therefore, for example, structures with a typical scale of $\sim$2.5 times the PSF have their central intensities dampened by a factor of $\sim$10, by contrast structures with scales of $\sim$7.5 times the PSF will appear $\sim$100 times fainter in the derivative map than in the original intensity map. Thus for a fixed threshold level on the same background, it is possible to identify, if they exist, structures with scales of the order of $\sim$2.5 times the PSF and intensities that are 10 times fainter than those with scales of $\sim$7.5 times the beam. It is clear that the closer the width of the structure to the scales of the background emission, the harder the structure will be to distinguish. They will stand out on the derivative images only if their intensities are comparable to that of the smallest scales present in the background component.

3.1. Unresolved Simulated Filaments

In Figure 3 we show an example of a simulation—the presented case has 25 filaments, all having a cross-spine size with FWHM of $\sim$3 pixels, namely the size of 1 PSF, corresponding essentially to unresolved filaments assuming a fully Nyquist sampled map, like the Hi-GAL maps (Molinari et al. 2010a). The set of filaments was distributed over three different patches of diffuse emission extracted from Hi-GAL 250 μm maps to try to make results independent from a specific local background condition. For each case, we normalized the mean intensity along the spine of the simulated filaments to the median value of the background in the patch to achieve a contrast level equal to one. Moreover, we also generated images where the brightness of the filaments was decreased by a factor of two and four with respect to the background image, to simulate filaments with different contrast levels (as an example we present the simulation with contrast 0.5 in Figure 3, top right). The filament extraction method is then applied over all simulated fields (25 filaments, for three different background configurations, for three different filament/background contrast ratios), using four different extraction thresholds. The code performances are characterized by comparing the length, width, and area of the recovered filaments with those of the input simulated ones.

Figure 4 reports the results for the recovered filament length as a function of the input length. Results are shown for the lowest (top row) and the highest (bottom row) extraction thresholds, and for decreasing filament/background contrasts (from left to right). On average, the results are very good, with recovered length that in most situations agrees with the input values within 20% for the range of thresholds adopted. In the case of the lower extraction threshold, we see a general trend to obtain lengths that are systematically overestimated by about 20% irrespective of the filament contrast. This can be explained by the fact that with low thresholds on the minimum Hessian eigenvalue the regions initially selected by the thresholding are larger, and the subsequent "thinning" systematically produces longer spines. The situation clearly improves going to higher thresholds for nominal and halved contrast ratios (Figures 4(d) and (e)) independent of the type of background used; if, however, the higher thresholds are used and the contrast gets too low (panel (f), a factor of four less with respect to the situation depicted in Figure 3), then the code starts to break the filaments up into shorter portions, depending on the background where the simulated filament falls. However the intermediate threshold

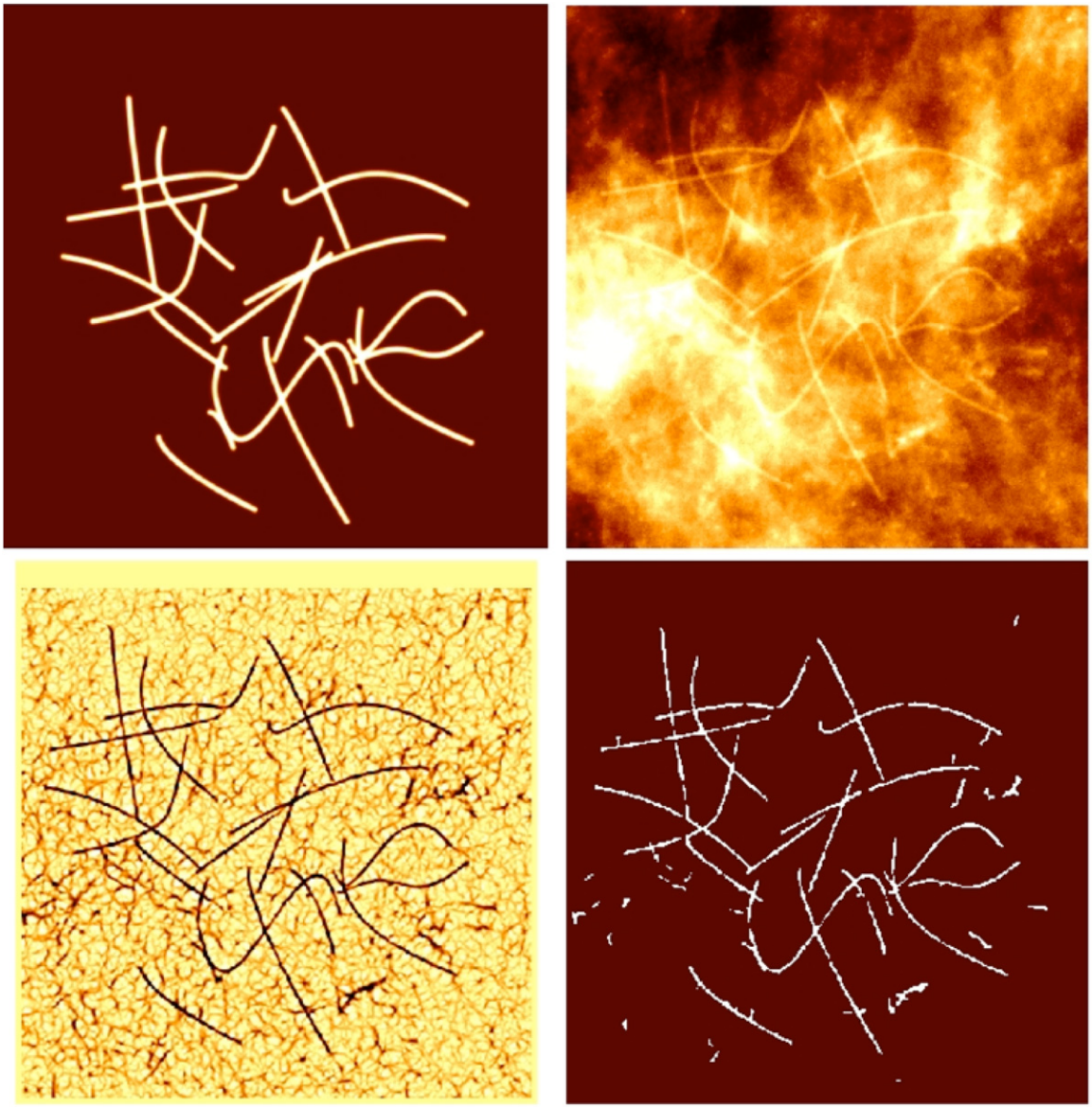

Figure 3. Results of the filament detection over a set of 25 simulated filaments with FWHM of three pixels in the top left panel, overlaid on a patch of emission from Hi-GAL 250 μm (top right panel) used as a background. Only the highest contrast filament/background situation simulated is reported in the figures. The bottom left panel shows the minimum eigenvalues image used for thresholding, while the bottom right shows the masks of the recovered filamentary structures; this shows more output filaments than the 25 input filaments because the background image used is real *Herschel* data from the Hi-GAL survey and as such contains real filaments.
(A color version of this figure is available in the online journal.)

lengths of the structures are still recovered within 20% accuracy even for this faint case.

The code behavior in recovering the average width of the filaments is more regular—independent of the extraction threshold, background type, and contrast—the recovered widths mostly agree better than 20% with respect to the input values.

An accurate estimate of the filament background is critical for a reliable measurement of the intrinsic filament emission, whether it is total flux or total column density (if run on a column density map). In Figure 5 we show an example of the reliability of our background estimates. We take a real field over the Galactic plane (top left) and superimpose a set of simulated filaments. We normalized the filaments to have contrast 1, 0.5, and 0.25 (only the case with contrast 0.5 is shown in the top-right panel). For the patch of background presented in Figure 5 the mean intensity along the filament spine is 35, 18, and 9 arbitrary units, respectively, for contrast 1, 0.5, and 0.25. We then extract the filamentary structures, identify the ones that correspond to the simulated filaments (these are the only ones for which we have a truth table), and subtract them. In the bottom left panel we show the difference between our estimate of the background after the subtraction of the filaments and the initial background (top left panel). The distribution of such differences between the input and the filament-subtracted backgrounds, for all the pixels where a simulated filament was inserted, is shown in the bottom-right of Figure 5 with a Gaussian fit overplotted in red. The distribution is centered around zero difference, with 95% of the pixels falling in the Gaussian fit with a FWHM of five in arbitrary units. The remaining 5% of pixels show residuals as large as 30 arbitrary units and are generally located at the bright position of the original background map (with values as large as 80 arbitrary units), sometimes on real compact sources, or where multiple filaments nest each other. Very similar distributions are found for all the contrast cases and depend mostly on the

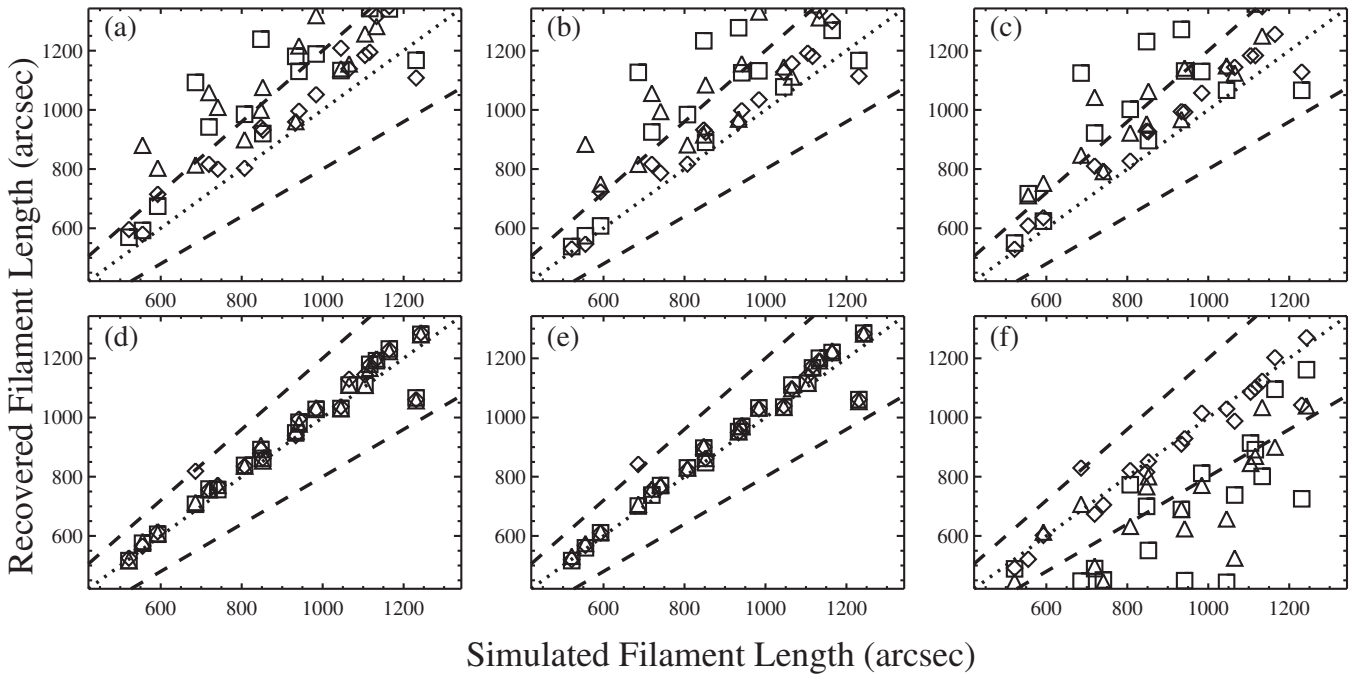

Figure 4. Results for the recovered filament lengths in the case of unresolved filaments vs. the true length. Each symbol represents one filament and the three different symbol types are for the three background types (see Figure 3). The top row is for the lowest used extraction threshold, which is more sensitive to relatively fainter structures; the bottom row is for the highest used threshold, which is less sensitive to fainter emission. For each row, the three panels show the results for the three filament/background contrast ratios used: in the left panel is the nominal situation that is represented in Figure 3, the center panel is for contrast reduced by a factor of two, while the right panel is for contrast reduced by a factor of four. In all panels the dotted line represents the identity line, whereas the dashed lines indicate a 20% discrepancy.

background, with residuals generally small with respect to the distribution of background intensities at the filament position. In other words, the code delivers reliable estimates of the filament underlying backgrounds.

3.2. Resolved Simulated Filaments

We further carried out simulations where the filaments are assumed to be resolved. Figure 6 is the analogue of Figure 3 for a different filament distribution, but in this case the filaments have a FWHM that is three times larger. As the intrinsic curvature will be lower for these extended structures, we expect the code performance to degrade accordingly. In fact, while the background has not been changed the filaments have a shallower intensity variation along the radial direction, so they are less prominent in the derivative image.

The recovered lengths for the retrieved filaments are shown in Figure 7, where the meaning of the symbols and the different panels is the same as in Figure 4. The code continues to perform very well on average, showing very similar behavior as for the unresolved features, up to moderate contrast between filament and background. For the lowest contrasted filaments simulated here, the code has more trouble recovering the correct length for low detection thresholds, producing a larger scatter of values (Figure 7(c)) than the unresolved case. In addition, at higher thresholds the moderate and low contrast filaments are also undetected, and the few detected ones are broken into smaller portions (Figure 7(f)). As expected, therefore, the shallower the structure this method, which is based on the second derivatives that are computed over a discrete set of pixels, performs less and less reliably. It is fair to point out that this breakdown in performance is experienced for very unfavorable conditions where the filament/background contrast is four times less than what appears in Figure 6. If the contrast is decreased by only a factor of two (Figures 7(b) and (e)), the code performs much better in recovering the length.

The situation is worse when one considers the widths of the filaments for the resolved case. As the features are much shallower than the unresolved filament case, while the spatial dynamical range of the background has not changed, the Gaussian fits performed at all spine positions are less constrained. The average result is that in the best contrast situations the width is systematically underestimated by about 20%. For lower contrast filaments the determination is much more noisy and the width is recovered with an uncertainty of the order of 30%–40%.

3.3. Filaments Widths and Background Estimates on a Real Filament

To prove in more detail the ability of our approach to recover a correct estimate of the filament width and background level, we illustrate the algorithm performance results on a real filament extracted from the more general results that will be presented in the following section. Figure 8 shows a typical real situation for a relatively isolated filament. We see that the average width of the filament as it would be estimated from the Gaussian fitting of the radial profile as explained in Section 2 (the dotted vertical line in Figure 8, right panel) is in excellent agreement with the cross-spine size of the final filament RoI (after applying the dilation operator), which corresponds to the left boundary of the gray shaded area in Figure 8 (right panel) and the black line in Figure 8 (left panel). The shaded area corresponds to the radial distance spanned by the pixels that in Figure 8 (left panel) are enclosed between the full and dashed black lines, where the background is estimated.

We point out that our method is totally consistent with classifying *as filamentary* all the pixels within the borders defined by the flattening of the radial profile. Such a definition

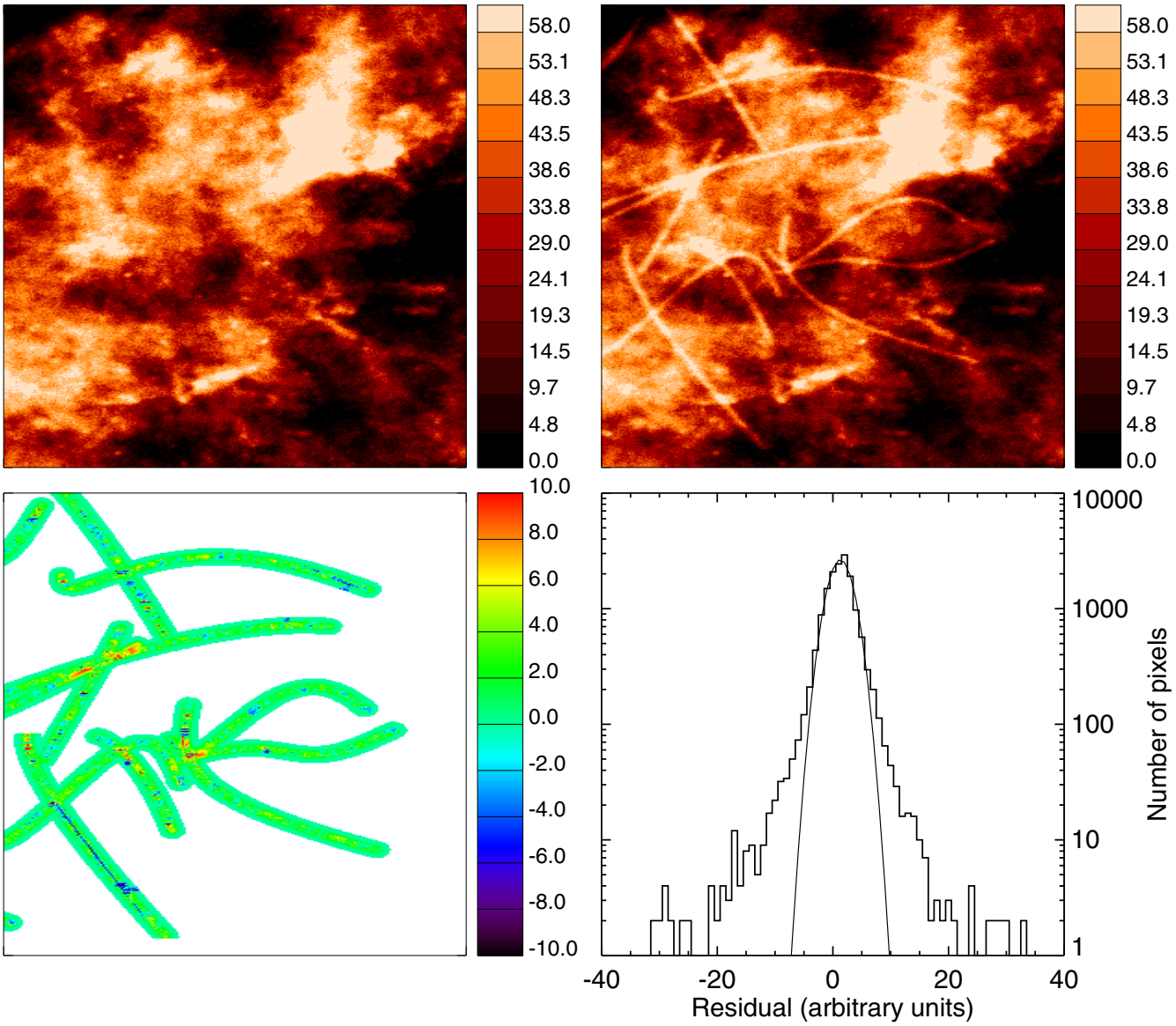

Figure 5. Typical field of the Galactic plane at 250 μm (top left), with a superimposed set of simulated filaments (top right); the colorscale provides the absolute signal levels of the map in arbitrary units. The simulated filaments shown here have a mean intensity value along the spine equal to 18 arbitrary units. The bottom left panel shows the difference between the background estimates at the filament positions and the original background. The bottom right panel shows the intensity distribution of the differences of the bottom left panel only for the pixels belonging to filaments. In red line we overlap the Gaussian fit to such distribution.

(A color version of this figure is available in the online journal.)

has already been used in previous works on filaments (i.e., Hennemann et al. 2012).

3.4. Performance Evaluation

The results of the extended set of simulations illustrated in the previous sections build confidence in the filament extraction method that we have developed. The method has been proved to easily identify structures that are as large as three times the hypothetical spatial resolution element of the test maps. It is clear that the best situation is for unresolved filaments, where the curvature of the brightness distribution is higher. Filament lengths and widths are in general recovered to within a 20% uncertainty with respect to input values, unless the filament/background contrast is very low. As expected, the situation gets worse when shallower filaments are used in the simulations. Whereas these fainter structures are still identified, the estimation of their morphological and physical parameters becomes unreliable. Similar uncertainties arise for wider simulated filaments, but with intensities that are comparable with that of the background component. Structures wider than three times the PSF are only identified if they are relatively bright with respect to the background. In such a case, the estimation of the parameters is satisfactory, due to the high contrast filament/background.

To summarize, the output of method is very reliable for structures as wide as three times the spatial resolution element of the map. However, the performances quickly degrade for wider structures that, due to intrinsic degeneracy in the method between the width and central intensities, can only be identified if they are as bright as the background. For a fixed threshold, the widest structure that can be identified depends on the background properties (its smallest scale and the relative intensity).

Another relevant point coming out of the simulations is that different thresholds are appropriate to highlight different kinds of structures—resolved/unresolved and with different contrast intensity—over different background values. While a high threshold value is able to properly recover unresolved

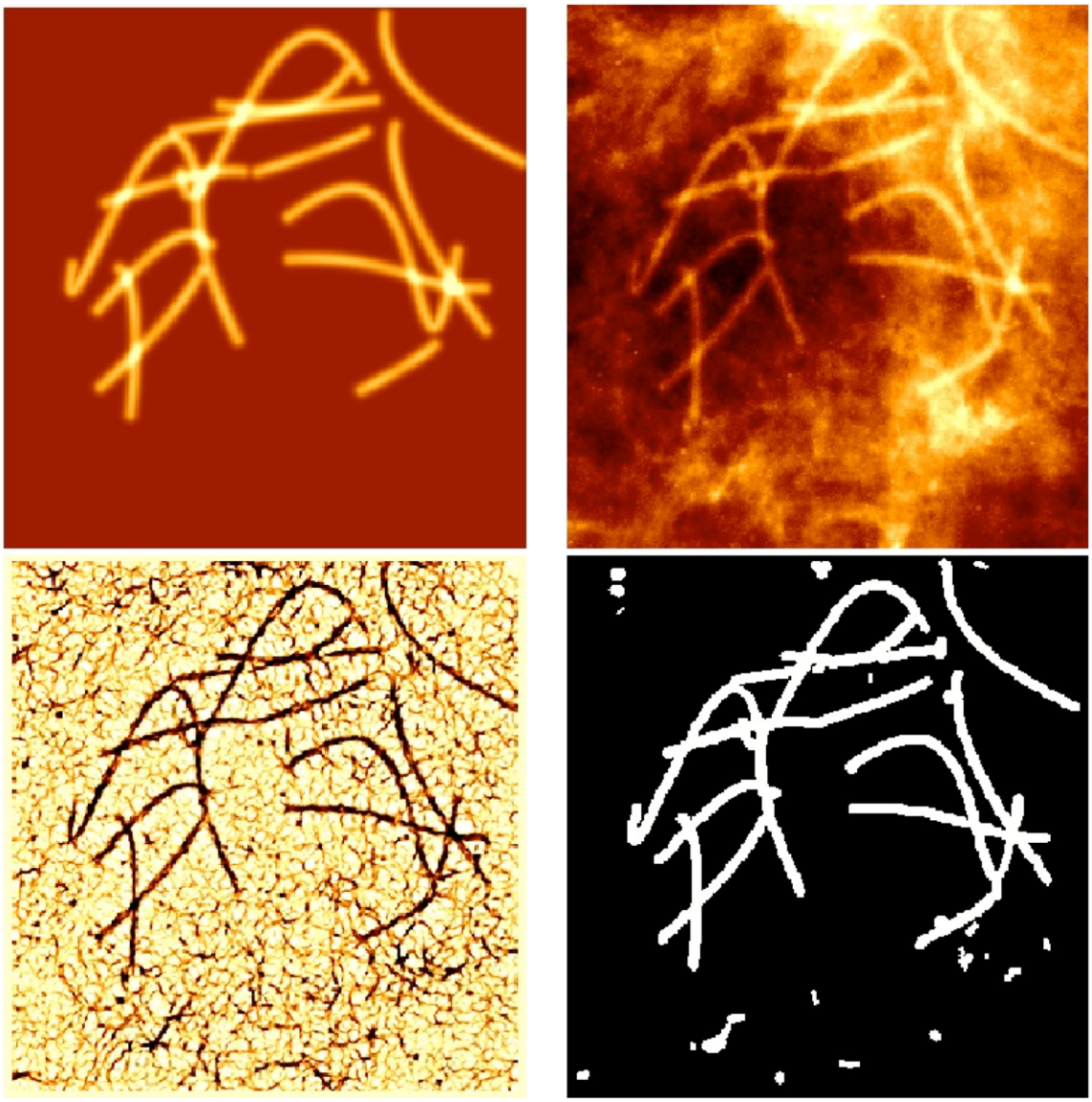

Figure 6. Same as Figure 3, but with filaments three times wider and differently distributed on the background image.
(A color version of this figure is available in the online journal.)

filaments with high/moderate contrast with respect to the background, it splits faint structures into multiple segments of shorter lengths. However, adopting a low threshold enlarges the identified RoIs and artificially increases the filament lengths in the high/moderate case. Ideally, we would like to apply a higher threshold on regions where the filament variations dominate over the background, and a lower threshold where they are shallower and fainter. Thus we adopt as a local estimator for the threshold the standard deviation of the minimum eigenvalue computed on map regions 61 × 61 pixels wide. Increasing the region size does not substantially change the minimum threshold value. This is expected, as by enlarging the region where the threshold is computed we are including the contribution from larger scales, which is negligible for scales greater than ∼60 pixels. In fact, those scales are dampened up to $\leqslant 0.5\%$ of their original value. With such a choice, the threshold will be higher in regions with large and intense fluctuations of the emission, eventually dominated by the presence of the filaments, whereas it will decrease in detecting regions with a shallower contrast where the variations are smaller.

Finally, it is worth noticing that while it is straightforward to identify filaments as elongated structures in the isolated cases, it clearly becomes difficult when multiple objects overlap each other, such as in the cases of our simulation. On real data, multiple filaments can be physically connected and converge toward larger structures, called "hubs" (Myers 2009), or crossing each other due to line of sight effects. From this point on, we will call *one filament* a whole region corresponding to one identified RoI. However, in the case of complex RoIs the axis is not a simple segment, but is often composed of multiple segments connected to each other in nodal positions. We call each one of those segments a *branch*. These branches reflect asymmetries of the RoI and have two different physical interpretations: (1) they represent the portion of a larger filament between two local overdensities inside the structure, and (2) they are physically separated filaments, connected to the main structure by our algorithm, since there is not a strong discontinuity in the contrast variation.

As an example in Figure 9 we show a $32' \times 17'$ wide region of the column density map centered at $(l, b) = (58.3917, 0.4235)$

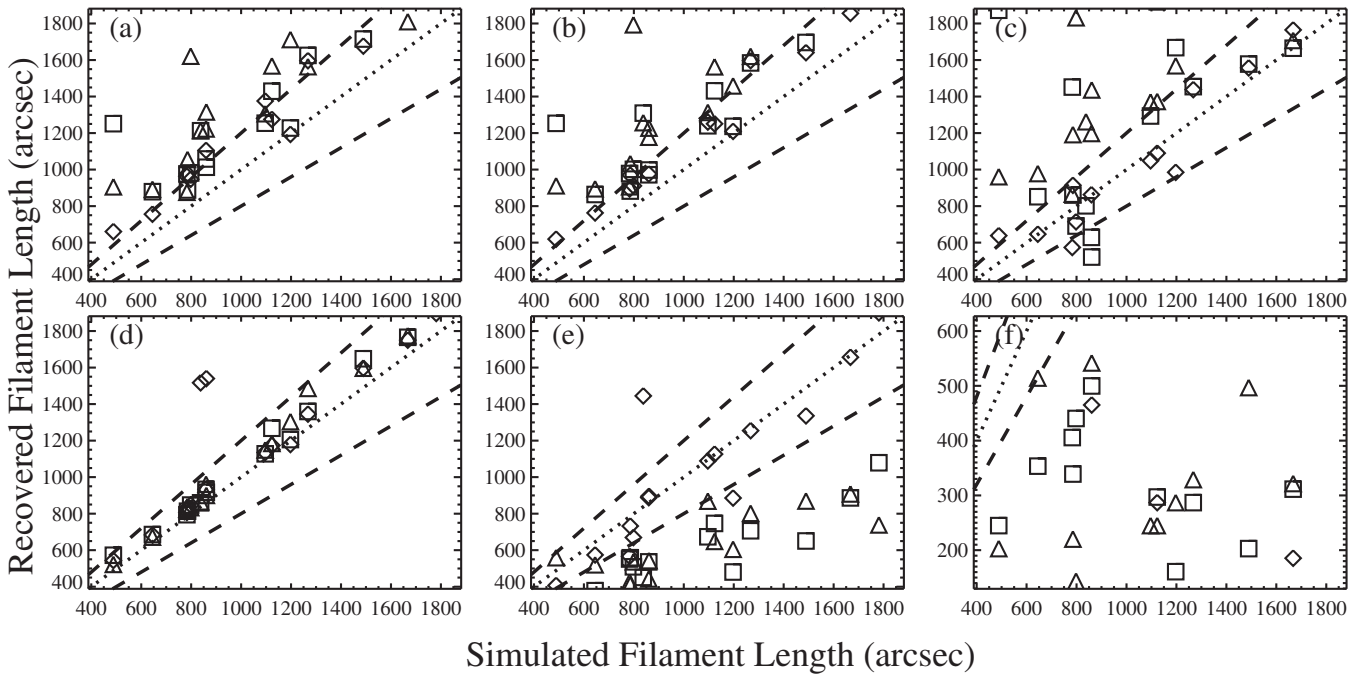

Figure 7. Same of Figure 4, but for the case of resolved filaments.

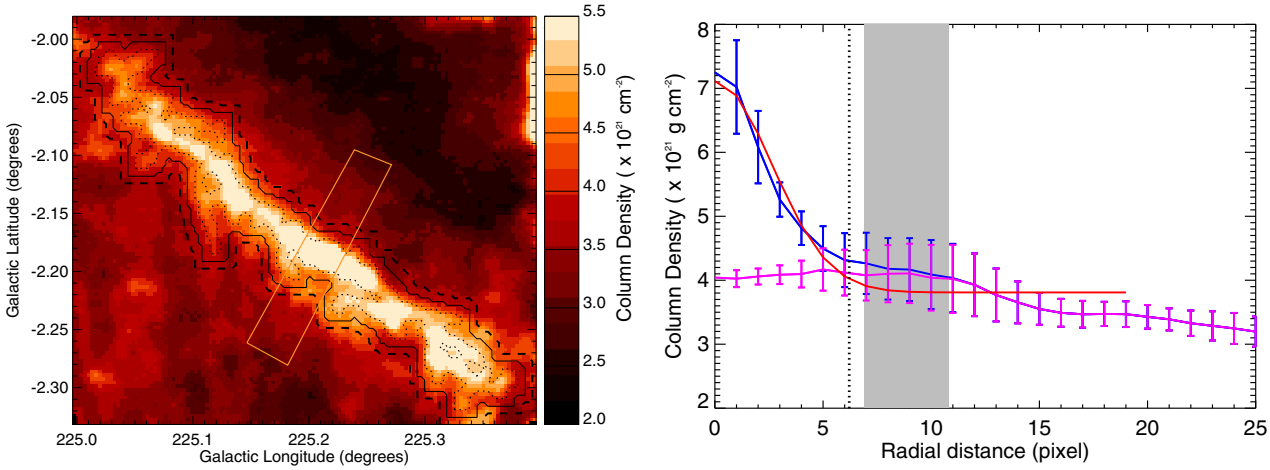

Figure 8. Left: subsection of the larger column density map of Elia et al. (2013) with a typical filament. The dotted line encloses the RoI selected by the initial thresholding on the Hessian eigenvalues; the full black line is the RoI after applying the dilation operator three times; the dashed line encloses the area over which the background is estimated. Right: cross-spine radial profile of the column density (blue line) for the region enclosed in the yellow-line rectangular area in the left panel. The full red line is the Gaussian fit, with the dotted vertical line marking a typical radial distance of one FWHM from the central spine. The full magenta line is the background profile estimated from the column density corresponding to radial distances falling into the shaded area.

(A color version of this figure is available in the online journal.)

computed from *Herschel* Hi-GAL observations. In this figure there are five filaments, only three of which, indicated by *B, C, D*, comprise a single axis. The two remaining, identified as *A* and *E*, comprise multiple branches starting from the nodal points, indicated with gray circles in the figure, and trace the main remaining structures.

The physical quantities for each branch, like mass or column densities, are computed on the sub-regions of the original filament mask determined by associating with each branch all the pixels that are closest to the relative branch spine.

4. DISCUSSION OF THE FILAMENTARY STRUCTURES IN THE OUTER GALAXY

Our filament identification algorithm was run on our column density map, which was calculated from the four *Herschel* Hi-GAL maps in the Galactic longitude range of $l = 216.^{\circ}5$ to $l = 225.^{\circ}5$, hereafter indicated as *l*217–224, at the wavelengths 160, 250, 350, and 500 μm. These maps were the first Outer Galaxy tiles published from the Hi-GAL survey. The *l*217–224 70 μm to 500 μm and column density maps were presented in Elia et al. (2013), along with a compact source catalog. The adopted dust opacity law was $k_0(\nu/\nu_0)^{\beta}$ with $k_0 = 0.1$ cm^2 g^{-1} at $\nu_0 =$ 1250 GHz (250 μm) (Hildebrand 1983) and β was assumed to be two. It is important to note that the dust opacity parameters adopted to compute the column density map are rather uncertain. The column density values depend on the assumptions in the dust emission model. For example, the fixed spectral index $\beta = 2$ might be wrong for the cold and denser regions, where a higher value for β is expected. A lower value for β influences the gray-body fit outputs with an overestimation of the temperature and an underestimation of the column density. Furthermore, a

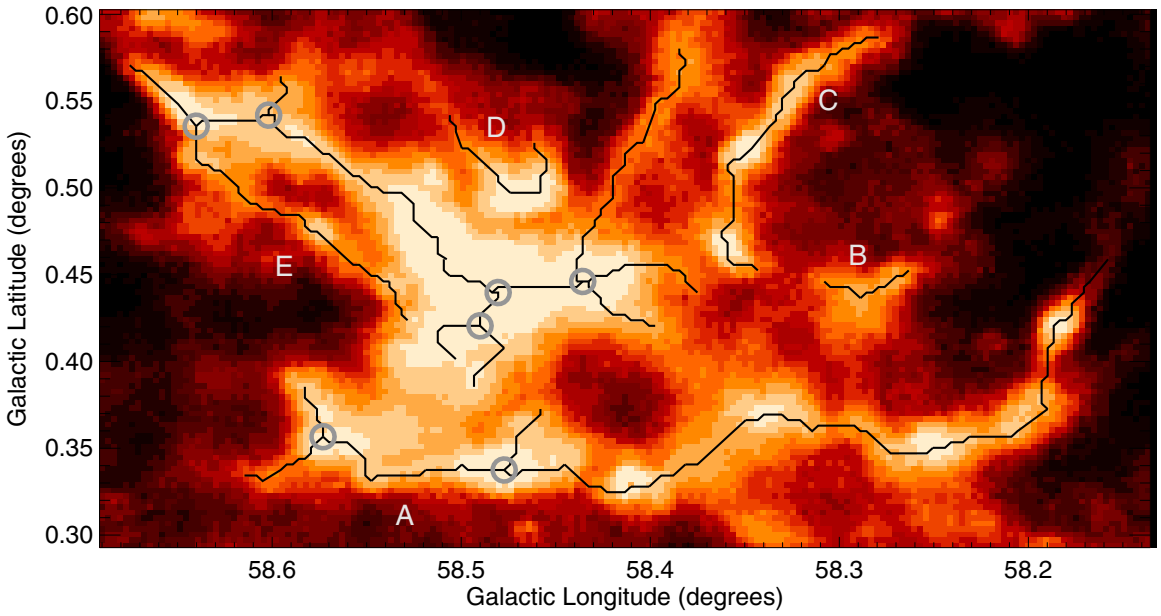

Figure 9. Column density map of a portion of the Hi-GAL observation centered at $(l, b) = (58.3917, 0.4235)$ and wide $32' \times 17'$. The axis of five filamentary regions, indicated by the letters from *A* to *E*, are shown as thick black lines. Filaments *A* and *E* are composed, respectively, by 5 and 12 branches connected to nodal points (indicated by gray circles in the figure).

(A color version of this figure is available in the online journal.)

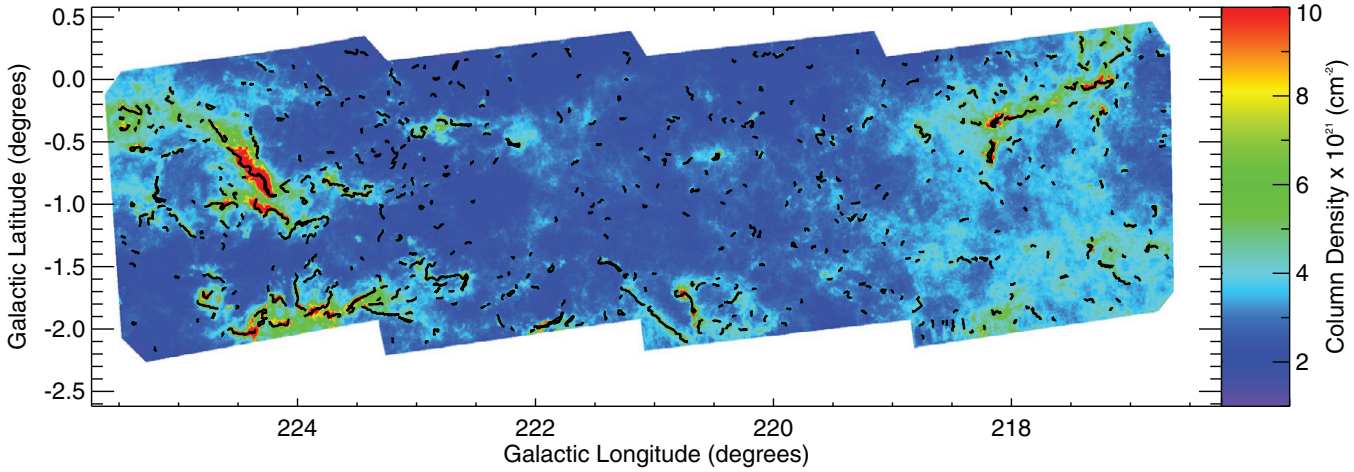

Figure 10. Column density map computed from the Hi-GAL maps in the Galactic longitude range from $l = 217$ to $l = 224$ presented in Elia et al. (2013). The thick black lines indicate the main spine of each detected filament. The detected filaments are the ones that show a variation of their contrast higher than three times the standard deviation computed locally on regions that are wide 11.7×11.7 arcmin^2 in size.

(A color version of this figure is available in the online journal.)

more realistic dust model can be adopted for the more diffuse material, see for example Compiègne (2010). We estimate that the uncertainty on the dust emission model can affect our estimate of the column density map by a factor of ∼two.

Elia et al. (2013) determined the kinematic distances of the compact sources in *l*217–224 from the CO (1–0) emission observed with the NANTEN telescope. Clump distances range from 370 pc up to 8.5 kpc and, as shown in Figure 3 of Elia et al. (2013), the degree of contamination from kinematically separated regions along the line of sight in the *l*217–224 longitude range is very low.

The filament extraction was run with a threshold of three times the local standard deviation of the minimum eigenvalue (see Section 3.4). Moreover, we filtered out any regions with a length smaller than four times the beam (i.e., ∼12 pixels or ∼2′) as further constraint on the ellipticity of the structure, in addition to that described in Section 2. By doing so we are excluding short, perhaps more distant, structures. Furthermore, as discussed in Section 3.4, we expect that our sample will be incomplete in terms of wide angular sizes. Moreover the detection algorithm can also miss narrow structures, if their contrast variation is lower than the adopted threshold. Farther filaments have a shallower gradient of the contrast along their profile due to beam dilution. This means the sample will also lack faint and narrow sources whose variation is closer to that of the background. Despite the incompleteness of the sample for more distant objects, our aims are to give a first estimate of the statistical properties of structures that look filamentary on *Herschel* maps. The shorter and fainter structures are statistically represented in our sample by the nearby structures. However, we remark that since the region studied in this work is mostly dominated by the emission coming from distances less than 1.5 kpc (Figure 3 and Table 1 of Elia et al. 2013), the incompleteness of the sample will have a minor impact on our results.

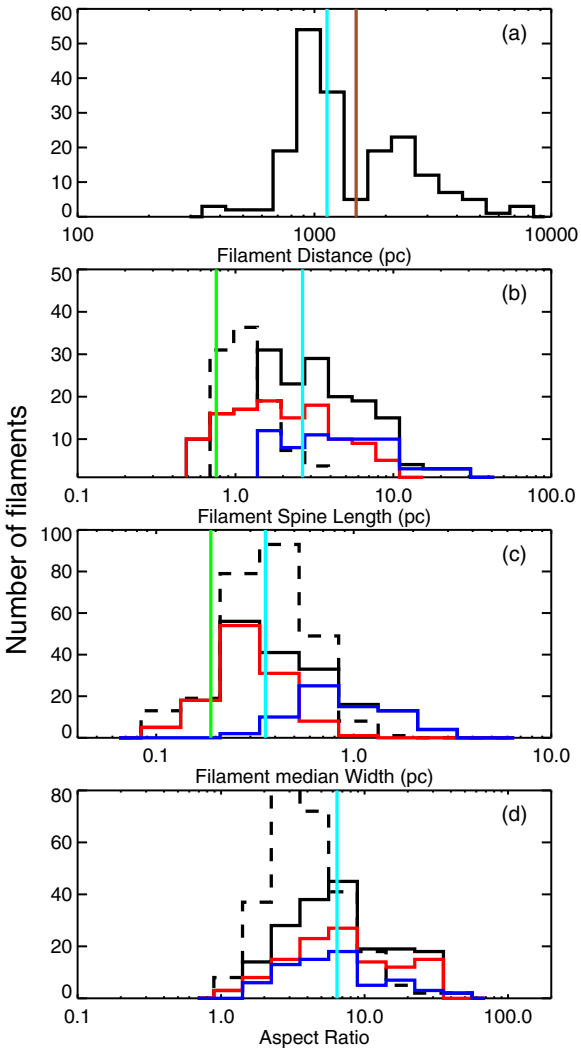

Figure 11. Distributions of filament properties: filament kinematic distance (panel (a)), filament length (panel (b)), measured width (panel (c)), aspect ratio (panel (d)) in the ∼500 filaments identified in the $l = 217$–224 longitude range. The cyan vertical line depicts the median value of filaments distance (1.1 kpc), length (2.5 pc), and aspect ratio (7.5). The red line in the panel (a) indicates the 1.5 kpc separation mark between the "near" and "far" sample (see text). In panels (b)–(d) we plotted in solid lines the spine lengths, and the width and aspect ratios for the filaments with a distance estimate, while the dashed line shows the histogram of the spine lengths and aspect ratios of the filaments for which we assumed the median distance of 1.1 kpc. Furthermore, we divided the sample depending their estimated distance in near ($d < 1.5$ kpc, plotted in red) and far objects ($d \geqslant 1.5$ kpc, plotted in blue). The green vertical line shows the length cutoff for filaments at 1.1 kpc.

(A color version of this figure is available in the online journal.)

4.1. Morphological Properties of Filaments

The algorithm identified ∼500 filaments that contain, in total, ∼2000 branches spread across the Galactic longitude range. The detected filaments are shown on the column density map in Figure 10. A visual inspection of the result indicates that all the major filaments identifiable by eye are traced by the algorithms.

We cross correlated each filament RoI with the clump positions from Elia et al. (2013) and, for the filaments with a match, we assigned the distance given by the mean value of the clump distances found within their border. We found that 40% of the detected filaments have at least one associated clump and their distances range from 500 pc to 8.5 kpc, with a median distance of 1.1 kpc (shown in Figure 11, panel (a)) corresponding to the average distance of the CMa OB1 association (Ruprecht 1966). The distance distribution is compatible with the two main Galactic arm structures along this line of sight: the Orion spur located at distance of $\leqslant$1 kpc and the Perseus arm at ∼2 kpc. Few filaments might be associated with the Outer arm, which is located at a distance ∼5 kpc, however we do not find a defined separation between filaments in such a structure and the one in the Perseus arm. The remaining 60% of the filament sample that were lacking a clear distance association were assumed to be at the 1.1 kpc (i.e., the median of the distribution; not shown in panel (a)). In the remaining panels of Figure 11, we plot separately the filaments with a kinematic distance (i.e., filaments with clumps) and these without (i.e., filaments without clumps) in solid and dotted lines, respectively. We point out that the percentage of filaments without a clump detection inside their border is affected by the criteria adopted by Elia et al. (2013). In fact, the catalog presented by these authors includes the clumps identified on the Hi-GAL maps for which they could determine a distance estimation, through a detection in the NANTEN CO observations. Hence, two effects contribute to the number of non-detected clumps inside the filament: the NANTEN observations (1) do not cover the whole area surveyed by *Herschel* Hi-GAL data (see Figure 4 of Elia et al. 2013), and (2) have a low sensitivity. We found that ∼10% of the detected filaments fall outside the NANTEN coverage area. Furthermore, we compared the maximum column density found in each filament RoI and estimated that another 8% of the sample are structures that might be undetected in the CO data.

The histogram of the filament spine length (for those filaments with a kinematic distance) peaks at around 2 pc, and despite the presence of a significant tail that extends up to 60 pc, most of the filaments have lengths between 1.5 pc and 9 pc, with a median value of 2.45 pc (panel (b), solid black line). The filaments whose distances were assigned to the median value show a different distribution (panel (b), dashed black line): their lengths strongly peak at 1 pc and then drop off quickly. The cut we have adopted in our selection criteria translates to an artificial length-cutoff at 0.74 pc for the median filament distance of 1.1 kpc. The lengths are estimated from the map and are liable to projection effects due to a possible inclination effect. No information is available for the possible inclination of these structures along the line of sight. Assuming a random uniform distribution for the inclination of the filaments, the observed mean value of the inclination angle with respect to the line of sight would be ∼57°, implying that the intrinsic filament length would be ∼19% longer. However, due to projection effects, we do not identify all the filaments that have a small angle between their axis and the line of sight, hence the true mean inclination would be larger. The net result is that the length distribution is closer to the intrinsic one.

In panel (c) of Figure 11 we show the distribution of the measured width for the identified structures. Almost all the filaments are resolved in their radial direction (see Figure 12) and only 8% of the filaments with a reliable distance have widths that are compatible within the errors with the beam size. We stress that the majority of detected filaments have a width ∼1.9 times the beam, despite simulations having shown that the method is more sensitive to unresolved "thin" filaments with respect to the resolved filaments, independently of the contrast. There is no apparent reason that far, unresolved structures should not be detected by the algorithm, as long they are not so shallow that they are confused with the variations of the background. We checked that the filtering of the sample on

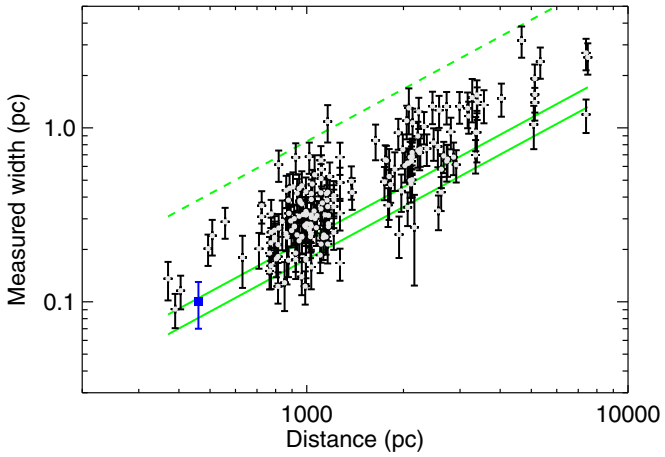

Figure 12. Measured width as a function of the distance for filaments with a reliable distance. For comparison, we also indicate with green lines the apparent size of an unresolved object with size equal to the theoretical beam (solid line on bottom), 1.3 times the theoretical beam (see the text for details—solid line on top), and five times such a value (dashed line) as a function of the distance. The blue square represents the median size of the filaments identified by Arzoumanian et al. (2011) in the IC5146 molecular cloud at a distance of 460 pc.

(A color version of this figure is available in the online journal.)

lengths, ellipticities, and filling factors does not systematically remove only the filaments with width of the order of the beam, and found that there is no net effect on the width distribution of the sample. Nevertheless, Figure 12 still shows a selection effect with the larger structures identified at farther distances. If the same filament population detected at about ∼1 kpc was shifted toward larger distances, we should detect a larger number of unresolved structures. Instead, if we compare the width distributions of the filaments separating the sample into distance bins, we found effectively a lack of narrow structures. Part of the reason should be attributed to the beam dilution that smooths more the variation of the density gradient for more distant objects, as discussed in Section 4, affecting the ability to detect the filaments with respect to the their surrounding emission. Furthermore, we analyzed the SPIRE maps and the column density map computed from them, which we adopted in this study, to search for structures with sizes of the order of the beam. We found that either for filaments or for compact sources there are a low number of objects whose width is close to the theoretical SPIRE beam. For the case of the compact sources identified by Elia et al. (2013) we found that the large majority of sources have a size that is ∼1.2–1.3 times the theoretical beam. A similar result is found almost everywhere in the galactic plane (see also S. Molinari 2014, in preparation). We explain this result, which is directly determined from measurements on the maps, as an effect introduced by the local halo in which the sources are embedded, which broaden the radial profile. In fact we note that the few cases compatible with the beam are generally well isolated objects on a very low background emission. A similar effect is also found for the filaments—the structures usually embedded in dense extended environment have a broader profile than the few isolated filaments. If we consider as unresolved all the filaments with a width within 1.3 times the theoretical beam size, we find that ∼20% of the whole sample is compatible within the errors with a structure not resolved in the radial direction. A similar percentage is found if the sample is split among filaments closer and farther than 1.5 kpc, showing that there is no significant statistical difference in the sample with the distance.

We computed the deconvolved widths for the resolved filaments and found a median width equal to 0.3 pc, a factor of ∼three larger than the one identified in nearby clouds (Arzoumanian et al. 2011).

The distribution of the aspect ratio, defined as the ratio between the filament length and its deconvolved width, is presented in Figure 11(d). The median value for the whole sample of filaments is 7.5, with the bulk of filaments having aspect ratios between 2 and 40.

The filaments we have identified on the Hi-GAL maps are typically longer and have higher aspect ratios than the filaments found by Hacar et al. (2013) in the L1495/B213 Taurus star-forming region, which have lengths ranging between 0.2 pc and 0.6 pc and aspect ratio between 2 and 7. Instead, the Hi-GAL filaments are similar to filaments identified by ammonia emission in more distant massive star-forming regions (i.e., Busquet et al. 2013 with lengths of 0.6–3.0 pc and aspect ratios of 5–20). It is not unexpected to find structures of different lengths when analyzing a whole portion of the Galactic plane. However we stress that, at least for the lower-contrast filaments, the measured lengths might be underestimated. Based on our simulations we found that some of the shorter filaments might belong to longer structures that were split into smaller portions by the adopted threshold in the filament extraction.

Our sample of filaments is spread over a wide range of distances, with the majority located around 1 kpc. Given the almost bimodal distance distribution around 1 and 2 kpc, we divided the sample, for which we know the distance through the association with clumps, into "near" distances for filaments with $d < 1.5$ kpc and "far" distances $d > 1.5$ kpc (see also the blue dashed line in panel (a) of Figure 11). There are almost twice as many filaments at "near" distances (121) than at "far" distances (70). The distribution of the "near" filament lengths has a mean of 2.6 pc with a standard deviation of 2.1 pc, whereas for "far" filaments the mean length is 6.9 pc and the standard deviation is 8.0 pc. "Near" filaments have more constrained spine lengths and are well represented by the main distribution seen in panel (b). The spine length of farther filaments has a larger spread across the histogram (panel (b)), however such an effect is mostly due to the cut on the size of the structure we have imposed in the extraction. In fact, the distribution shows a cut-off at ∼1.4 pc, corresponding to our filter length of ∼2′ for the median distance of 2.45 kpc if we consider only the sample at the "far" distance. Our filter length implies that, depending on the distance, we are missing structures with lengths between 1.4 and 4.6 pc, the latter being the shortest filament we would keep for the distance of 8.5 kpc. The filament (deconvolved) widths show a similar trend: nearby filaments widths are narrower and well confined, the distribution has a mean of 0.26 pc and a standard deviation of 0.16 pc, whereas farther filaments have wider widths with a larger spread, with a mean of 0.82 pc and standard deviation of 0.57 pc. Again the effect of the distance justifies the two different shapes of the distribution.

4.2. Probability Density Functions of Column Density

Figure 10 strongly suggests that the filaments are denser structures with a certain morphology, sometimes embedded in a less dense molecular cloud. Hence, before discussing the average physical properties of the identified filament sample, we discuss the probability density functions (PDFs) of column density to quantify the difference between the filamentary

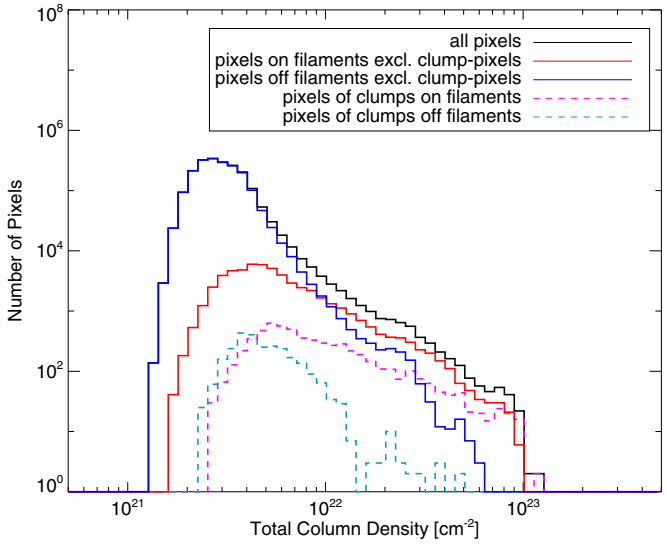

Figure 13. Column density map pixel distributions. Pixels associated with a filament constitute the violet histogram, Pixels not associated with filaments constitute the blue histogram.

(A color version of this figure is available in the online journal.)

structure and the more diffuse material. PDFs are a useful tool for detecting the presence of density structures (e.g., clumps and cores) in molecular clouds. A lognormal distribution of column densities is usually taken as proof of an isothermal medium where significant large-scale turbulent motions are taking place (Vázquez-Semadeni & García 2001), whereas the departures from that, generally identified as power-law tails in the high column end of the distribution, are a sign that self-gravity is starting to take hold (Kainulainen et al. 2009) or, equally feasible, for the presence of a non-isothermal turbulence (Passot & Vázquez-Semadeni 1998).

The global PDF of the *l*217–224 region has already been discussed in Elia et al. (2013), here we continue the analysis dividing the region into on- and off-filament. Furthermore, we separate the PDFs for pixels containing clumps from those without for both filamentary and non-filamentary regions, by flagging all the pixels within a HPBW of the clump position for each clump. Such a separation quantifies how much the clumps contribute at the high column density end of the distribution, where we expect a strong contribution from gravitationally bound structures.

Figure 13 shows that the shape of the distributions of filamentary (without clumps) and non-filamentary (with clumps) regions are clearly different. The off-filament pixels follow a lognormal distribution at low column densities, with a power-law at higher column densities. The peak of the distribution is at $N_{\rm H_2} \sim 2.5 \times 10^{21}$ cm^{-2} representing the column densities of the diffuse galactic material in the outer galaxy (see also Figure 10). While the filaments' pixels have a less pronounced lognormal distribution peaking at higher column densities ($N_{\rm H_2} \sim 4 \times 10^{21}$ cm^{-2}), they have a much more dominant power-law tail at high column densities. Below the limit of $N_{\rm H_2} \leqslant 4 \times 10^{21}$ cm^{-2} only 1% or less of the pixels in the column density map lie in filaments. Column densities with 4×10^{21} cm$^{-2} \leqslant N_{\rm H_2} \leqslant 6 \times 10^{21}$ cm^{-2} are clearly dominated by the non-filamentary molecular cloud emission. For $N_{\rm H_2} \geqslant 6 \times 10^{21}$ cm^{-2} the majority of the pixels fall in filamentary regions.

Clumps on filaments dominate the high column density end, as expected, but do not account for the entire power-law tail. Hence, the dense material contained in the filament, but not in the clumps, may indicate that the filament itself is not dominantly made of isothermal material. A possible explanation is the presence of some clumps not identified in the previous analysis, while a more suggestive hypothesis would be that self-gravity is taking over not only in the clumps but also in some portions of the filament. In other words, the presence of such high density regions might indicate that filaments are part of a globally collapsing flow. Our data are not conclusive to determine if this hypothesis is correct and further investigation through spectroscopic data is needed. In fact, Schneider et al. (2010) and Kirk et al. (2013), in analyzing the molecular line profiles found hints of global collapse and accretion onto the filaments in nearby star-forming regions.

The pixel distribution of the clumps off filaments does not dominate at the high column density end ($N_{\rm H_2} \geqslant 2 \times 10^{22}$ cm^{-2}), but at intermediate column densities (3×10^{21} cm$^{-2} \leqslant N_{\rm H_2} \leqslant 2 \times 10^{22}$ cm^{-2}). It is likely that the high column density end of the off filament distribution belongs to the dense molecular cloud surrounding the filamentary structures (see also Figures 14 and 15).

4.3. Filaments Column Densities

We have identified filaments in the *Herschel* data as isolated structures, as well as parts of a more complex structure: the denser parts of a molecular cloud, see Figure 10. For every pixel in each filament, we defined the contribution to the measured column density from the filament as the difference between the pixel value, given by the gray-body fit of the 160–500 μm fluxes, and the local estimated background given by the interpolation along the direction orthogonal to the filament spine (see also Section 3.3). Figures 14 and 15 show some examples of filaments (in the left panels) and the estimated background (in the right panels). Panels (a) and (b) in Figure 14 (the latter shows the same filament of Figure 8) are isolated filaments that include the majority of the material, while in panels (c) and (d) in Figure 15 the identified filaments are deeply embedded in the cloud. Denser filaments are found in the denser environment, as shown also in Figure 16, suggesting a scaling relationship between the mean density of the background and the matter accumulated into the filament.

We show in Figure 17 the histogram of the *mean* value of the filament contribution to the column density, adopted in the following as an estimate of the average column density of the filament. Our filament sample covers a range of average column densities, from 10^{19} cm^{-2} up to 10^{22} cm^{-2}. We divide the sample into three groups: "*A*" filaments with at least one associated clump and therefore with a kinematic distance, "*B*" filaments without any association and lacking distances, and "*C*" filaments with unknown association (see Section 4.1), still lacking a distance determination.

Filaments with clumps are clearly denser (the median value is 4.8×10^{20} cm^{-2}) than those without (median equal to 1.7×10^{20} cm^{-2}). The distribution of filaments in group "*A*" and "*B*" are very different and the probability P_{AB}, obtained with the Kolmogorov–Smirnoff statistic, that the populations are drawn from the same distribution is very low ($P_{AB} \ll 1 \times 10^{-5}$). Moreover, we computed either the probability that the population with unknown association "*C*" could be drawn from the distribution of filaments with clumps, P_{CA}, and the probability that "*C*" could be drawn from the filaments without clumps, P_{CB}. We found that the population "*C*" is significantly different from both, $P_{CA} \ll P_{CB} \sim 10^{-4}$, however,

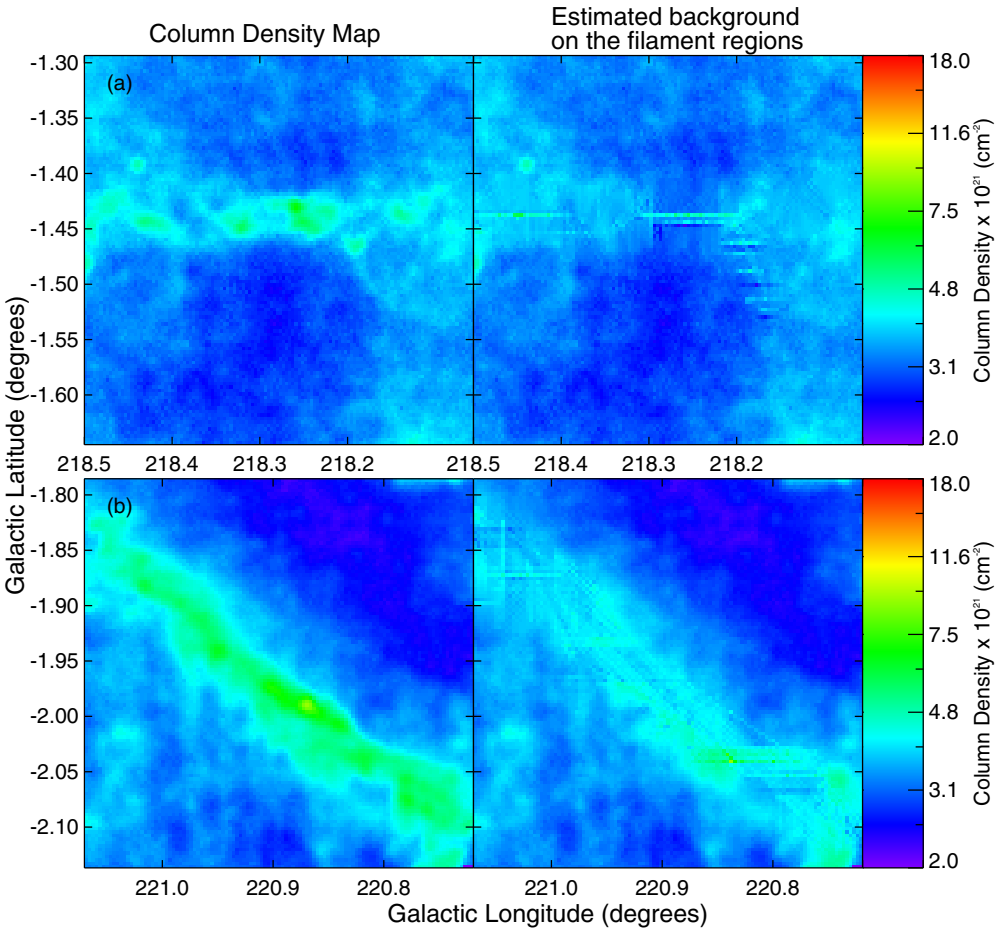

Figure 14. Examples of filaments. In the left panels we present the original column density map where the filaments are identified, while in right panels we show the estimated background on the filaments. The top panels (a) and (b) are examples of isolated filaments, while panels (c) and (d) are filaments embedded in the denser environment of a molecular cloud.

(A color version of this figure is available in the online journal.)

the large difference between the two probabilities seems to indicate that this sample is composed mostly by filaments without clumps. We conclude that the differences between the populations "*B*" and "*A*" are real and not due to the lack of distance determination. The filaments in population "*B*" did not form clumps because the column densities were too low.

Despite the column density being a *distance independent* quantity, it can be influenced by beam dilution in unresolved or low filling factor sources. Given that one observes a structure with the same physical size, one expects lower column densities at farther distances when beam dilution plays a role. As in Section 4.1, we divided the sample into the "near" and "far" populations and overplotted the corresponding histograms in Figure 17. Indeed, we found that the average column densities for nearby filaments are higher and with a larger spread (the distribution has a mean of 9.7×10^{20} cm^{-2} and a standard deviation of 14.0×10^{20} cm^{-2}), whereas at larger distances filaments have lower column densities and a smaller spread (the distribution has a mean of 6.8×10^{20} cm^{-2} and a standard deviation of 7.5×10^{20} cm^{-2}). Given the small differences between the mean values of the two samples, it appears that beam dilution has a small effect on *the average column density estimator*. This is especially true considering that most of the filaments in our sample are resolved in the radial direction and have lengths several times larger than the beam.

Our estimates of the column densities are generally lower than the ones found by Arzoumanian et al. (2011) in nearby star-forming complexes. However, we point out that they report the central column densities, which are always higher than the mean value of the overall structure. To compare these quantities we also estimated the central column densities from the pixels of the filament spine, which do not belong to individual compact sources, after the subtraction of the estimated background. The maximum central column densities measured are a factor 5.8 ± 2.4 higher than the average filament column densities. However, the maximum values for the column densities along the spine might be influenced by undetected sources and/or by local density enhancement. In the same way, the mean and the median are affected by the low column density pixels, still traced by the code, connecting different potions of the filament through regions where the material has been partially removed. If we adopt as estimator the 3rd quartile of the distribution of the column densities along the spine, background subtracted and not belonging to the sources, we would find that the central column densities are higher by a factor of 3.1 ± 1.2 than the average column densities. With the adoption of these factors, we again find that our central column densities are comparable with the ones found with *Herschel* by Arzoumanian et al. (2011) in nearby star-forming complexes ($N_{\rm H_2} \sim 10^{21}$ cm^{-2}).

Finally, we want to emphasize some caveats related to our estimation of the filament contribution to the column density.

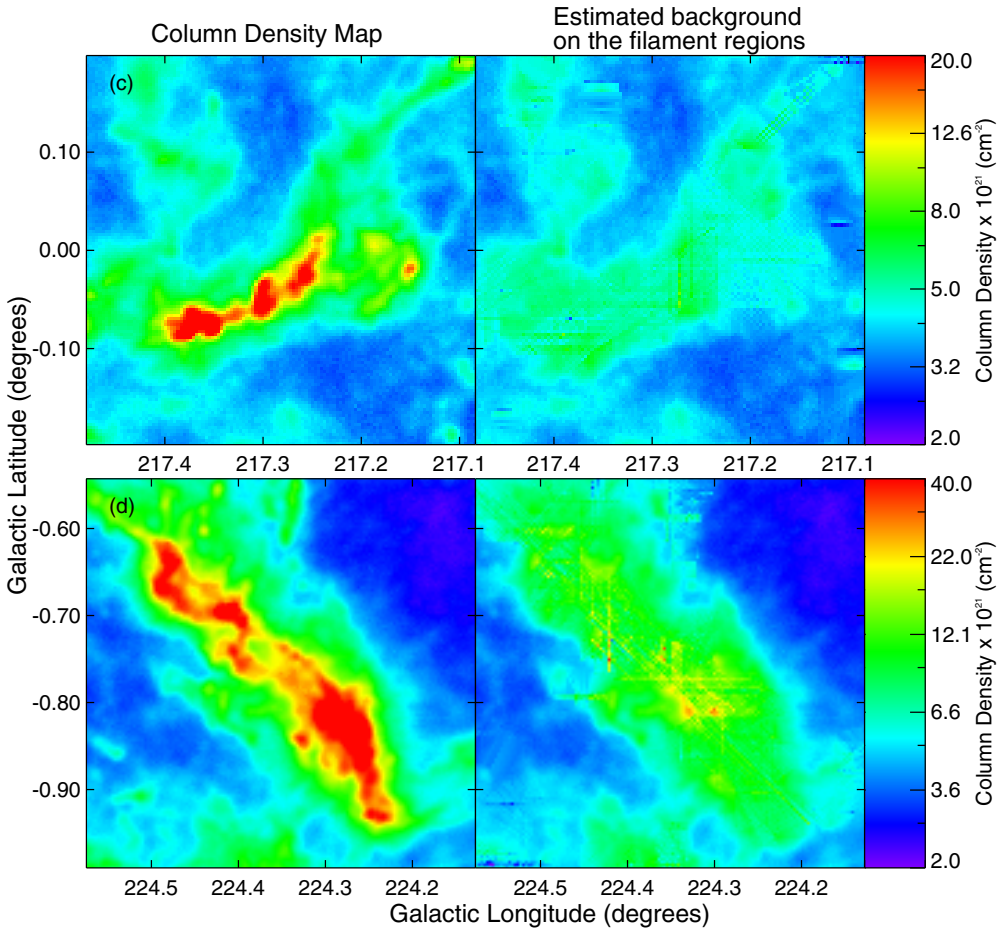

Figure 15. As in Figure 15, but for the case of filaments embedded in the denser environment of a molecular cloud.
(A color version of this figure is available in the online journal.)

First, in every pixel the column density values are affected by beam dilution, which smooths the density enhancements in the central part of the filaments. Second, when we compute the filament contribution after subtracting an estimate of the background, which consists of diffuse emission from the Galactic plane and/or the underlying surrounding material, we are implicitly assuming that the background and filament add linearly to give the calculated column density. Strictly speaking this is only true when both components have roughly the same temperature. However, this condition is generally not satisfied, especially in the denser regions, which are typically colder than their backgrounds. The overall effect is that the assumed filamentary column density contribution in a *single pixel* is an underestimate of the real column density, with larger discrepancies found at higher column densities.

Both beam dilution and the uncertainty due to the single temperature approximation affect the estimate of the central column density with respect to the average column density defined at the beginning of this section. Hence, in the following sections, all the derived quantities related to column density have been estimated using the average value.

4.4. High-mass Star Formation in Filaments

Elia et al. (2013) performed a thorough study of the star-forming content of the *l*217–224 longitude range of the Hi-GAL data. They identified the compact sources (clumps) and classified them as protostellar, prestellar, or unbound clumps.

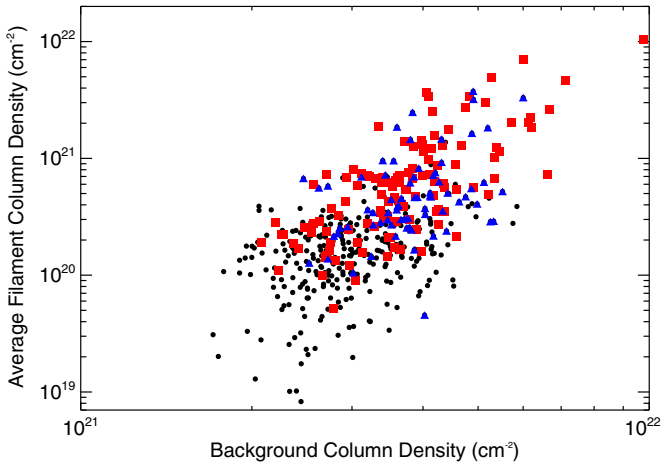

Figure 16. Filament background column density against average filament column density after subtracting the background, red squares indicate filaments with distance $d < 1.5$ kpc, while blue triangles indicate filaments $d \geqslant 1.5$ kpc. The black dots indicate the filaments without an associated distance arbitrarily assigned at distance $d = 1.1$ kpc (see the text for details).
(A color version of this figure is available in the online journal.)

Protostellar objects are objects that contain 22 and/or 70 μm emission, indicating the presence of young stellar objects (YSOs). The remaining starless objects, which do not contain a YSO (no 22 or 70 μm emission), can be divided into prestellar objects—gravitationally bound objects that are evolutionarily

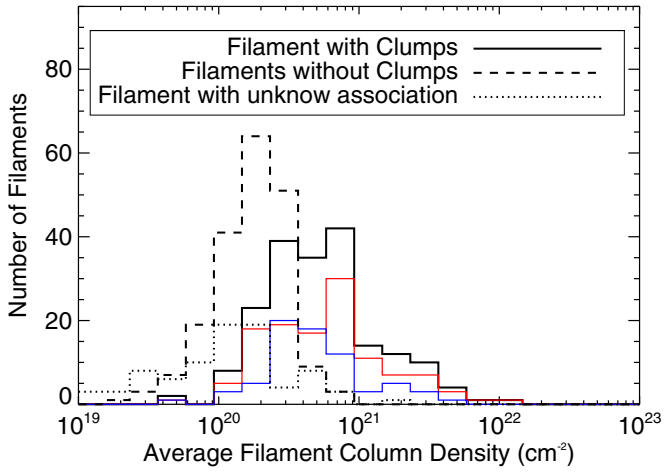

Figure 17. Histogram of filament column density for filaments with and without clumps. The sample has been divided in three groups, filaments with clumps, filaments without clumps, and filaments where the association is uncertain (see the text). Furthermore, the filaments with clumps have been separated into "near" ($d < 1.5$ kpc—plotted in red) and "far" ($d \geqslant 1.5$ kpc—plotted in blue) filaments. The black dots represent filaments without a distance estimate for which we assumed a distance $d = 1.5$ kpc.

(A color version of this figure is available in the online journal.)

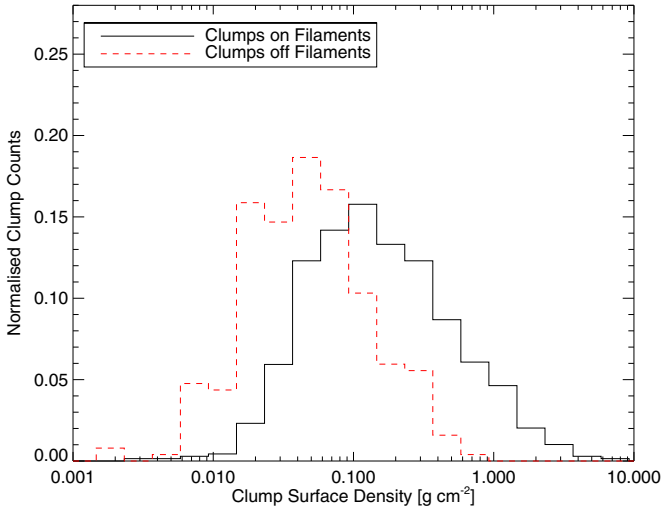

Figure 18. Clump surface density distribution for clumps located within filaments and clumps not located within filaments.

(A color version of this figure is available in the online journal.)

younger than protostellar ones—and unbound starless objects by comparing their mass, M, with their Bonnor–Ebert mass, $M_{\rm BE}$ (see Elia et al. 2013 for a detailed discussion). Here we adopted the criteria of $M > M_{\rm BE}$ to separate the prestellar objects from the unbound starless ones.

We correlate the above clump classification with our filament sample to understand the impact of filamentary structure on the star formation activity. The overall result shown by Figure 17 is that the filaments with hints of star formation are dense, with higher average column density values (distribution peaking at $0.5 - 1 \times 10^{21}$ cm^{-2}) than those without star formation, whose average column densities peaks at 2×10^{20} cm^{-2}. The differentiation starts at 4–6 $\times$ 10^{20} cm^{-2} (see Figure 17). Moreover, we found that not all filaments have clumps. If we exclude from the sample the filaments for which the clump detection might have been biased due to the NANTEN observation coverage and sensitivity, we find that 50% of the detected filaments do not have clumps. These filaments without clumps are in a very early stage of evolution or, alternatively, they might be transient structures, only confined by the external pressure.

Not all the remaining filaments show signs of ongoing star formation, in fact filaments with only unbound starless clumps (4% of the sample) do not contribute to it.

Polychroni et al. (2013) investigated the fraction of sources *on* and *off* filament in the L 1641 clouds in the Orion A complex and found that 67% of the prestellar and protostellar sources are located on a filament. In our case, which includes several molecular clouds, we find a similar fraction with the majority, 74%, of the clumps reported by Elia et al. (2013) falling within our filament sample. However, there are still a significant number of clumps detected off filaments.

We computed the clump surface densities from the masses and radii reported in Elia et al. (2013) and compared clumps located on filaments, $\Sigma^{\rm on}$, and those not on filaments, $\Sigma^{\rm off}$ (see Figure 18). The distribution of $\Sigma^{\rm on}$ peaks around 0.1 g cm^{-2} and reaches values up to 10 g cm^{-2}, while $\Sigma^{\rm off}$ peaks below 0.1 g cm^{-2} and reaches a maximum value of $\sim$0.8 g cm^{-2}. The shape of the two distributions is statistically different, with a more evident tail toward higher surface densities for sources on filaments. The different shapes might be explained by the larger uncertainties of $\Sigma^{\rm on}$ due to the difficulties in decoupling the compact source contributions from the underlying structure. However, we estimate that such uncertainties are up to $\sim$30%, while to match the two distributions would need $\Sigma^{\rm on}$ to be overestimated by a factor of $\sim$three. Therefore, it is very likely that the sources on the filaments have larger surface densities than the ones outside. More important, we observe that all the sources lying outside the filamentary regions have surface densities smaller than $\Sigma \sim 1$ g cm^{-2}. This value is advocated in theory of the star formation through turbulent accretion as the threshold limit below which the *massive* stars cannot form due to fragmentation. Recent observations indicate that such a threshold limit should be revised to a lower value of $\sim$0.2 g cm^{-2} (Butler & Tan 2012). Even with this revised limit, our results suggest that it is favorable to form massive stars in the filamentary regions.

Similar conclusions were reached by Polychroni et al. (2013) from the analysis of the clump mass functions (CMFs) for *on* and *off* filament sources. They found that the CMF of *on*-filament sources peaks at higher masses ($\sim$4 $M_\odot$) than the *off*-filament ones ($\sim$0.8 $M_\odot$), suggesting that the discrepancy is caused by the larger reservoir of material available locally on filaments in respect to the isolated clumps.

4.5. Stability of Filaments

Given that filaments can be roughly approximated as cylinders, theory shows that such structures have a maximum linear density, or mass per unit length $M_{\rm line}$, above which the system would not be in equilibrium against its self-gravity. For the simplified case of a cylinder infinitely extended in the z-direction with support given only by thermal pressure, the critical mass per unit length, $M_{\rm line,crit}$, is only a function of temperature (Ostriker 1964; Larson 1985). It becomes a more complicated function when other effects like turbulence and/or magnetic fields are taken into account (Fiege & Pudritz 2000), in this case the $M_{\rm line,crit}$ will increase by a small factor. Structures with an $M_{\rm line}$ above the $M_{\rm line,crit}$ will start collapsing along the radial direction. The critical mass per unit length scales linearly with the temperature and its value is around $M_{\rm line,crit} \sim 16\ M_\odot$ pc^{-1}

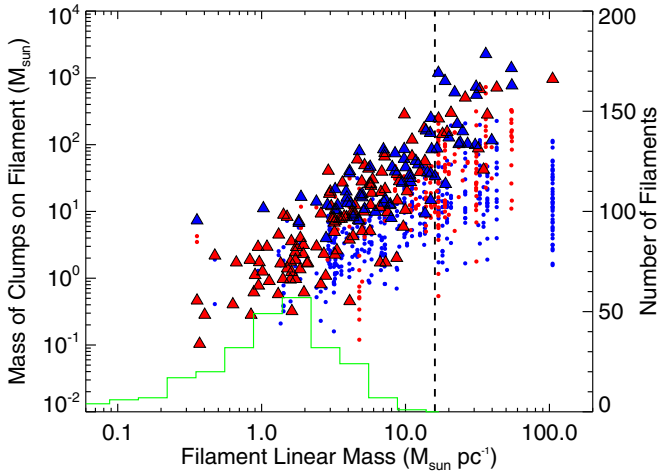

Figure 19. Mass of the clumps inside a filament as function of the hosting filament mass per unit length. Small dots are individual clump masses divided in red for near filaments (distance $d < 1.5$ kpc) and blue for far ones (distance $d \geqslant 1.5$ kpc). Triangles depict the total mass in clumps on that filament. For comparison, we also plot the filaments without clumps (green histogram) to show their distribution in mass per unit length. The vertical dashed line marks the critical mass per unit length $M_{\rm line,crit} \sim 16\ M_\odot\ {\rm pc}^{-1}$ for $T \sim 10$ K.

(A color version of this figure is available in the online journal.)

for the typical temperature in molecular clouds of $T \sim 10$ K, (see for example André et al. 2010). We estimated the mass per unit length for each detected filament from the average column density in the RoI, which is given as the sum of the contribution from the filament (see Section 4.3) divided by the area of the RoI, multiplied by the mean width. In the simple case of a straight filament—aligned on the plane of the sky with no density variations along the spine and constant radial profile along the structure—the estimator defined above equals the integration along the radial profile divided by the length of the structure (i.e., the mass per unit length). The unknown inclination of the structure affects our estimate of $M_{\rm line}$. However, while on the one hand the area of the filament projected on the plane of the sky is reduced due to projection effects, on the other the measured column density will increase by ∼60% for the same reason. The two effects partially balance each other.

For the more complex filaments detected in this field there might be small discrepancies. We stress that our definition entails an average (global) $M_{\rm line}$ for the whole filamentary structure. In other words, we are assuming *the total mass measured in the entire structure was initially uniformly distributed along the filament when it formed*. Therefore, even if we determine low values of $M_{\rm line}$ we cannot exclude that locally, in a small portion of the filament, the density is enough to become gravitationally unstable.

Figure 19 shows the mass of the clumps identified in the filaments with respect to $M_{\rm line}$. We have excluded from our analysis the filaments with starless clumps that have no contribution in terms of star formation. We additionally show the distribution of $M_{\rm line}$ for those filaments without clumps (green line): all filaments without clumps have $M_{\rm line} < 10\ M_\odot\ {\rm pc}^{-1}$, i.e., smaller than $M_{\rm line,crit} \sim 16\ M_\odot\ {\rm pc}^{-1}$. Filaments with clumps span a much wider range of values, with $M_{\rm line}$ up to $100\ M_\odot\ {\rm pc}^{-1}$. Many filaments found in the *l*217–224 field have $M_{\rm line} < 16\ M_\odot\ {\rm pc}^{-1}$, and so are subcritical ($M_{\rm line} < M_{\rm line,crit}$), even though they contain clumps. We stress that the value of $16\ M_\odot\ {\rm pc}^{-1}$ should not be taken as a strict limit, as real filaments (1) might not be correctly described by isothermal model and (2) have a finite extension along the z-direction. Hence, even in the case of finite slightly "subcritical" filaments, it is expected that both the external pressure and the gravity play a role.

The distribution of $M_{\rm line}$ for filaments with clumps (see Figure 19) indicates that many filaments did not initially have supercritical $M_{\rm line}$ to begin the clump collapse and star formation. If we assume that $M_{\rm line}$ remained unchanged during the onset of star formation, then this implies that gravity alone was insufficient to cause a global collapse into clumps. Moreover, the ability to form clumps with lower or higher masses is inherent to the initial $M_{\rm line}$ of the filament: more massive clumps form in the more critical (and supercritical) filaments. Since this last result might be biased by including the contribution of the clumps to the average column density, we estimated the $M_{\rm line}$ by excluding the clump mass contribution to the identified filament. This estimator represents the stability of the remaining material in the filament against gravitational collapse, and for a filament where the star formation process is complete it can be lower than $M_{\rm line,crit}$. The trend shown in Figure 19 does not change with removing the clumps from the $M_{\rm line}$ calculation, indicating that the relation between $M_{\rm line}$ and the clump mass is real.

Finding filaments hosting clumps with an average $M_{\rm line}$ lower than the critical value is not completely surprising. Our filaments are comparable to infrared dark clouds (IRDCs) and high-extinction clouds that often display a filamentary morphology and are generally found to have distances of 2–4 kpc (see for example Rathborne et al. 2006; Rygl et al. 2010). Recently, Hernandez & Tan (2011) and Hernandez et al. (2012) investigated the dynamical state of two IRDCs and found $M_{\rm line} \simeq 0.2$–$0.5 M_{\rm line,crit}$. While their analysis is based on molecular line data, taking into account the (stabilizing) non-thermal contribution to the $M_{\rm line,crit}$, they find clear signs of star-formation activity, through the presence of 8 μm and/or 24 μm point sources, in gravitationally stable structures. More generally, molecular clouds, and also filamentary molecular clouds, are found overall to be gravitationally unbound when their masses are compared to the virial mass, despite the fact they contain gravitationally bound clumps and star formation (Rygl et al. 2010; Hernandez & Tan 2011). The general idea is that these large-scale structures are not far from virial equilibrium and that external pressure or flows could have initiated the star formation activity (Tan 2000). Therefore, while the external pressure is confining the larger structures, the smaller scales (found locally) have to be supercritical to show hints of star formation activity (André et al. 2010). The sweeping up of interstellar material and its accumulation in large-scale filamentary structures through converging flows (Heitsch & Hartmann 2008; Vázquez-Semadeni et al. 2011) is compatible with such results, forming the large structure and initial local overdensities at the same time. Our results indicate that these processes have to act quickly, on timescales shorter than the filament and clump free-fall timescales. If that were not the case, supercritical filaments with $M_{\rm line} > M_{\rm line,crit}$ would have a larger number of clumps, as further clumps form as a result of the filament contraction and fragmentation. We do not find such an evidence in our sample. Even though it is difficult to confirm the converging flow scenario without kinematical information or shock tracing molecules, such as narrow SiO emission, (Jiménez-Serra et al. 2010), our data encourage the further investigation of these converging flows. Furthermore, we expect that all the supercritical filaments are characterized by a state of global gravitational collapse, such as the DR 21 filament

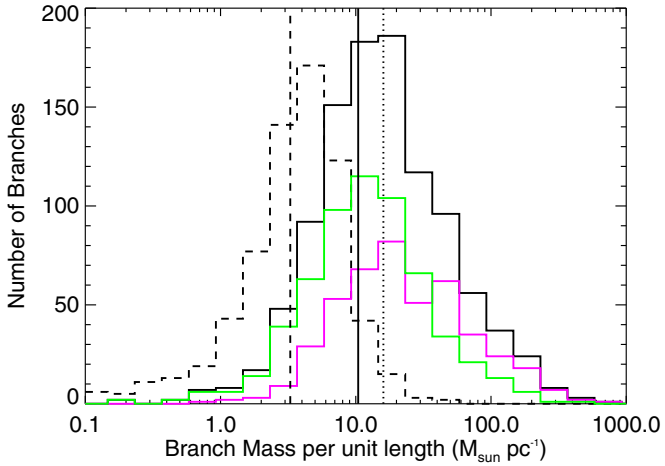

Figure 20. Histograms of branch mass per unit lengths for the branches belonging to filaments with clumps (solid black line) and filaments without clumps (dashed black line) with their median represented as vertical lines. The branches belonging to filaments with clumps are further split into branches hosting clumps themselves (magenta line) and branches without clumps in their local surrounding (green line). The dotted line indicates the $M_{\rm line,crit}$ value of 16 $M_\odot$ pc^{-1}.

(A color version of this figure is available in the online journal.)

(Schneider et al. 2010), where the molecular line observations strongly suggest the convergence of large-scale flows as the cause of its formation (Schneider et al. 2010; Csengeri et al. 2011).

4.6. The Nature of Filaments

In the previous section we concentrated on average global quantities measured on the whole filamentary structure. However, as explained above, the evidence of subcritical filaments with hints of star formation requires the presence of local instabilities inside the filament. Therefore we focus the following analysis on filament branches (see Section 3.4 for the definition), which give more local information than the global averages described so far.

Figure 20 shows histograms of the branch $M_{\rm line}$ after separating the branches into the filaments hosting clumps from the branches in filaments without clumps. The branches belonging to filaments with clumps have higher linear densities (median $M_{\rm line} \sim 10\ M_\odot$ pc^{-1}) than the ones without (median $M_{\rm line} \sim 3.3\ M_\odot$ pc^{-1}). Furthermore, we split the branches within filaments with clumps on the basis of their local association with clumps (in green) or not (in magenta). We found that the branches without clumps, but belonging to filaments with clumps, have still larger linear densities (with a median $M_{\rm line} \sim 10\ M_\odot$ pc^{-1}) than the branches without any clumps in their surroundings. It is unlikely that this difference is due to the distance association, even if the $M_{\rm line}$ depends linearly on the distance, since we found that a similar relationship exists for the branch average column densities. The branches with clumps are denser with a median $M_{\rm line} \sim 17\ M_\odot$ pc^{-1}. They dominate the distribution for $M_{\rm line} \geqslant 16\ M_\odot$ pc^{-1} (the equilibrium limit against fragmentation for an isothermal cylinder at 10 K, dotted line), despite the fact there are still a few branches without clump closer to $M_{\rm line,crit}$.

We have further refined the division in Figure 20 by specifying the branches that contain protostellar objects, prestellar objects, and branches without clumps in the top panel of Figure 21. For this last case, we took only the branches where we can determine

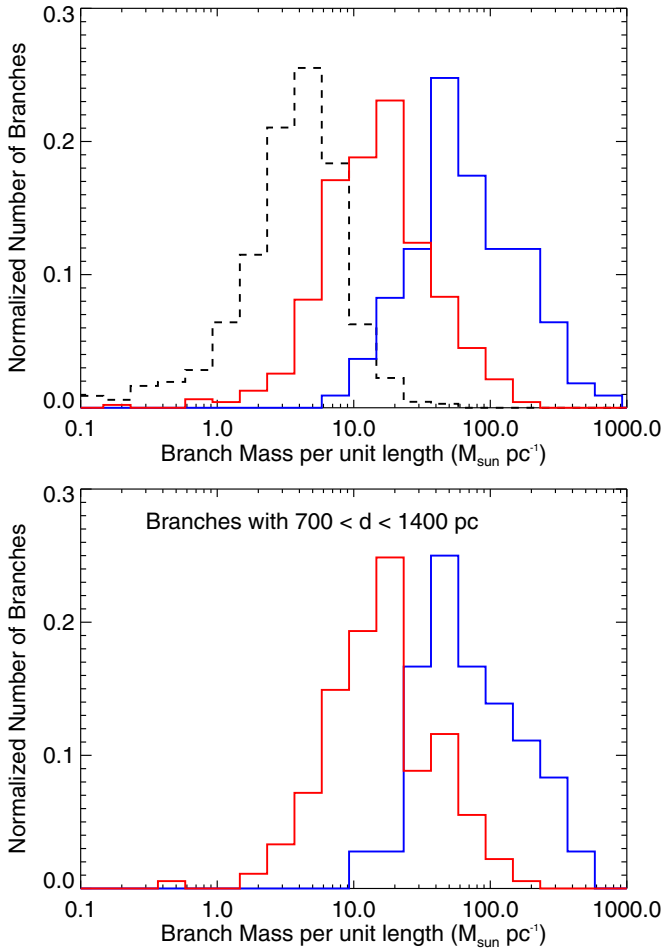

Figure 21. Top panel: histogram of masses for unit length of all the branches with protostellar clumps (blue solid line), with prestellar clumps (red solid line), and branches without clumps (black dot–dashed line). Bottom panel: distribution of masses for the unit length of the branches with associated distances between 700 and 1400 pc with protostellar clumps (blue solid line) and prestellar clumps (red solid line).

(A color version of this figure is available in the online journal.)

a distance through filament association to avoid any bias that might result from the assumed distance. The classification of a branch is based on the most evolved object found within, hence, branches that contain both prestellar and protostellar objects have been considered as branches with protostellar objects. With this definition, the total number of branches with an associated clump divides into 20% classified as protostellar and 80% classified as prestellar. We found that branches with protostellar clumps have the highest $M_{\rm line}$ with a median value of $\sim$60 $M_\odot$ pc^{-1}, which is well above the critical mass per unit length of 16 $M_\odot$ pc^{-1}. Branches with prestellar clumps have a median $M_{\rm line} \sim 15\ M_\odot$ pc^{-1}. We further checked if our results are affected by systematic effects due to the distance, since we are integrating on larger volumes for more distant filaments. In the bottom panel of Figure 21 we select only the branches of the filaments that fall in the range between 700 and 1400 pc. We chose such an interval to have a statistically significant number of objects. The difference in $M_{\rm line}$ between the branches with protostellar clumps and the ones with prestellar clumps is maintained. In such a distance range we found 180 branches (84% of the total) with prestellar clumps and 36 (16% of the total) with protostellar. We tested different distance ranges and

found that the branches with prestellar clumps always have a distribution with a median between 10 and 14 $M_\odot$ pc^{-1}, while the median of the distribution of branches with protostellar clumps varies between ∼40 and 70 $M_\odot$ pc^{-1}. The number fraction of branches classified as prestellar is always four to five times larger than the ones classified as protostellar. We conclude that distance selection effects are not affecting our result.

The analysis of the local $M_{\rm line}$ confirms that almost all the branches hosting protostellar clumps are locally unstable against gravity, despite the possibility of the overall filamentary structure being potentially subcritical. The branches belonging to filaments with clumps have a higher $M_{\rm line}$ with respect to the branches in filaments without clumps, with values closer to virial equilibrium. Thus, clump formation is somehow linked to the properties of the large-scale filament and, although this result might be affected by undetected clumps on the filament, the filaments hosting clumps are locally different than the ones without. Furthermore, we interpret the strong differentiation in $M_{\rm line}$ for branches with prestellar and protostellar objects shown in Figure 21 in terms of an evolutionary scenario, in which the protostellar branches are intrinsically more evolved than prestellar branches. This result indicates that $M_{\rm line}$ might *not* be constant during the onset of the star formation, as also suggested by Heitsch et al. (2009). In such a scenario the branches and their filaments increase their linear density with time by contracting and/or accreting material. The idea of mass accumulation with time is consistent with observations of velocity shifts along filaments (Peretto et al. 2013; Kirk et al. 2013). Moreover, *Herschel* observations of filaments in the Taurus star-forming region revealed substructures ("striations") connected to the filament along perpendicular directions with respect to the filament axis (Palmeirim et al. 2013). These authors suggested that the presence of such structures hint that the accumulation of mass is going on.

Our data indicate that the branches would have to increase their linear density by ∼45 $M_\odot$ pc^{-1} (given by the difference between the medians of the two distribution) on the timescale of prestellar evolution until the first protostars form. Unfortunately prestellar lifetimes are very uncertain, Motte et al. (2007) suggested that they last for 10^3–10^4 yr depending on the mass of the clumps, and with the assumption of a constant accretion rate. However, observations of nearby clouds indicate that there are a similar number of prestellar and protostellar cores, suggesting they have a similar lifetime of the order of 4.5×10^5 yr (Ward-Thompson et al. 2007; Enoch et al. 2008). The same lifetime of $\sim 10^5$ yr is estimated from numerical hydrodynamical simulations (Galván-Madrid et al. 2007; Gong & Ostriker 2011). Hence, our results require an accretion rate of $\sim 10^{-4}$ $M_\odot$ pc^{-1} yr^{-1} to match the measured higher linear densities in the filamentary region with protostellar clumps. Such accretion rates are possible and they are lower than that estimated by Kirk et al. (2013), both for accretion *along* the filament or for accretion *from* the environment. Recently Gomez & Vazquez-Semadeni (2014) analyzed filaments that form in simulations where colliding flows are responsible for the initial cloud formation. They found that filaments accrete from the environment and simultaneously accrete onto the clumps within them. They determine linear density increments up to $\sim 3 \times 10^{-5}$ $M_\odot$ pc^{-1} yr^{-1}, a few times lower than the value we estimate. However, we point out that they are analyzing structures that are ∼15 pc long, while our results are estimated from the measure of the local branches, which are a smaller portion of the filaments.

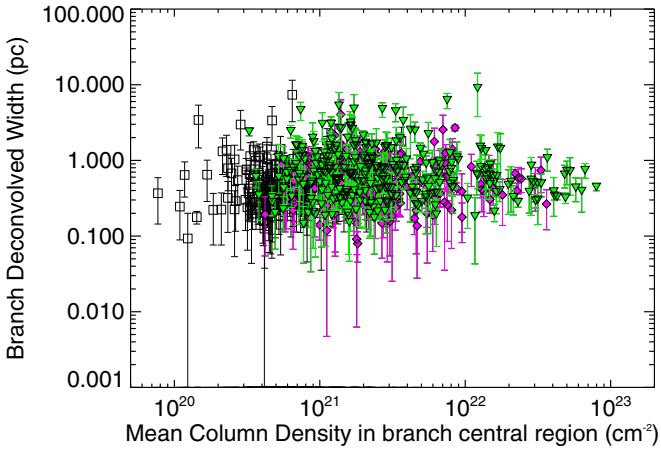

Figure 22. Mean column density measured along the central region of the branch excluding the overdensities due to the clumps vs. the deconvolved width for branches belonging to filaments without clumps (black empty squares), branches without clumps but belonging to filaments with clumps (green triangles), and branches with clumps (blue diamonds).

(A color version of this figure is available in the online journal.)

The observed increase in linear density in our sample could be explained by a contraction of the filaments by gravity. In such a case the shrinking of the filaments would be evident from the structures with a higher central column density having smaller widths. Figure 22 shows the branch deconvolved width, W, as a function of the average column density along the branch spine excluding the source contributions, $\overline{N^c_{\rm H_2}}$. No hints of correlation between the width and the $\overline{N^c_{\rm H_2}}$ is found, regardless of whether we analyze branches with or without clumps. We obtain similar results if we select only the branches in a small range of distances to minimize the possible impact of missing narrow, unresolved, or wide, but faint, structures. Thus we rule out that the contraction of the filament is responsible for the increase in linear density. A similar result was found by Arzoumanian et al. (2011) for the filament sizes in nearby star-forming regions and these authors adopted it as evidence in favor of the large-scale turbulence scenario for the *formation* of the filaments. In fact, if filaments were formed as a result of gravitational collapse and the fragmentation of an *isolated sheet* (Inutsuka & Miyama 1992), then W should be anticorrelated with $\overline{N^c_{\rm H_2}}$ and should be equal to the thermal Jeans length $\lambda_J = c_s^2/(G\mu m_{\rm H}\overline{N^c_{\rm H_2}})$, which is inconsistent with what is found. In contrast to Arzoumanian et al. (2011) whose average width is ∼0.1 pc, we measure an average filament width of ∼0.5 pc in accordance with the sizes measured for some filamentary IRDCs (Jackson et al. 2010). Such a larger average width has dynamical implications for these structures. If we assume that the filament width is roughly equal to the effective Jean length $\lambda_J^{\rm eff} = \sigma_{\rm tot}^2/(G\mu m_{\rm H}\overline{N^c_{\rm H_2}})$, where $\sigma_{\rm tot}$ takes into account both thermal and non-thermal contributions, we do expect that the supercritical filaments need a larger non-thermal contribution to hold their sizes in comparison to the smaller structures identified in nearby star-forming regions (Arzoumanian et al. 2013). An additional contribution to the velocity dispersion with respect to the one initially given by the large-scale turbulence in the interstellar medium was already suggested by Arzoumanian et al. (2013). In our case, either these structures are formed through the turbulent scenario with larger non-thermal support, or they require a larger contribution from the accretion. We want to stress that, since $M_{\rm line} \sim \overline{N^c_{\rm H_2}} \times W$, the larger average widths imply a lower value of

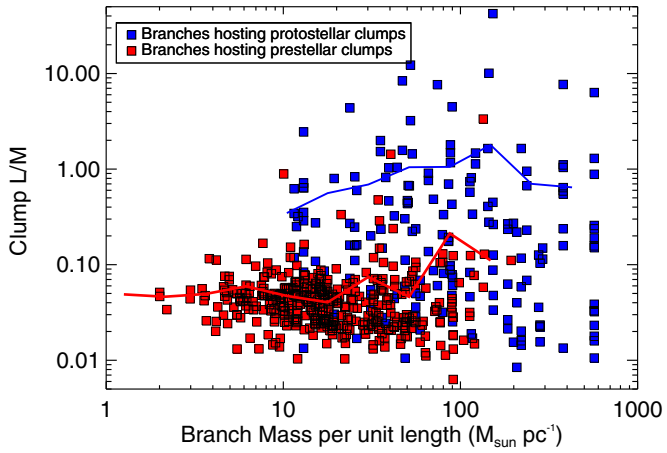

Figure 23. Branch mass per unit length vs. clump L/M ratio, with a separation between the branches hosting only prestellar clumps and the one with at least one protostellar clump. The lines represent the mean of the L/M distribution in logarithmic bin of size 0.2 dex.

(A color version of this figure is available in the online journal.)

central column density to reach the critical value of $M_{\rm line,crit} \approx 16\ M_\odot\ {\rm pc}^{-1}$. Thus, we estimate that the critical central column density, excluding any non-thermal support, is $\sim 1.8 \times 10^{21}\ {\rm cm}^{-2}$, implying that accretion has to be present in all regions of the filaments with $\overline{N^c_{\rm H_2}}$ above such value. However, such results have to be confirmed through direct measurements of $\sigma_{\rm tot}$ inside these regions, that is beyond the reach of the current NANTEN data.

Finally, in Figure 23 we plot the L/M ratio of the clumps versus the mass per unit length, separating the protostellar clumps (blue squares) from prestellar clumps (red squares) to provide an evolutionary marker for the objects forming in the branches. The L/M ratio is usually correlated with the evolutionary state of a forming star (Molinari et al. 2008). In this star-formation model, two phases are considered: (1) the mass accretion phase, in which the stellar object accretes from its massive envelope and increases its luminosity. This phase ends when the stellar object arrives at the zero age main sequence and becomes a star. (2) The envelope dispersion phase, in which the envelope mass decreases while the luminosity stays constant. Assuming that all the objects belong to the same initial mass function, and that each clump forms a single object, one can use the L/M ratio to distinguish between more and less evolved objects.

The prestellar clumps have a constant mean L/M ratio of $\sim$0.06 covering a range of local $M_{\rm line}$ between 1 and 100 $M_\odot\ {\rm pc}^{-1}$. The L/M dispersion increases for $M_{\rm line} > 10\ M_\odot\ {\rm pc}^{-1}$ due to the presence of prestellar clumps with $L/M > 0.1$. Almost no prestellar clumps are found in branches with $M_{\rm line} \geqslant 100\ M_\odot\ {\rm pc}^{-1}$. The protostellar clumps have a higher L/M ratio, with a median value $\sim$1, and present a larger scatter than the prestellar clumps. All the branches hosting the protostellar clumps have $M_{\rm line} \geqslant 10\ M_\odot\ {\rm pc}^{-1}$.

If evolution is the only mechanism in action, we do expect to find higher L/M ratios in branches with higher $M_{\rm line}$. A tentative increase of L/M can be drawn at least for the supercritical branches that appear to be more evolved than the subcritical ones. However, the large dispersion in the L/M suggests that the scenario is not complete. In particular, we cannot exclude the possibility that the branches have a different star formation rate and, therefore, the clumps would have different values of L/M despite having a similar evolution history.

We found very few branches that are highly supercritical ($M_{\rm line} \geqslant 100\ M_\odot\ {\rm pc}^{-1}$). Surprisingly, they host very few prestellar clumps, whereas we would expect a larger number due to the filament fragmentation, since they evolve on faster timescales than the filament (Toalá et al. 2012). It is possible that the already formed clumps have a strong effect on the filamentary structure through outflows and other feedback mechanisms, while the filaments themselves are still accreting material from the surroundings. Such feedback changes the local properties of the filament and prevents the further formation of clumps. The end result is that the filament would be dissipated rather quickly. This would explain the larger number of branches with prestellar objects versus the ones with protostellar objects. Therefore, filamentary structures are rather short-lived entities.

5. CONCLUSIONS

In this paper we have described a method to identify filaments of variable intensity from 2D in an automatic and unbiased way, taking into account the extended nature of these structures. The method has been optimized to work for the typical properties of filaments observed by the *Herschel*, with filaments overlapping, a strong and variable background, and hosting compact sources. With the help of simulations, we have shown the strengths of our approach not only as a way to detect, but as a tool to determine the morphological and physical properties of the filaments. Lengths and widths are typically recovered within 20% of the expected value. Larger discrepancies are found in the case of fainter, less contrasted, structures. We stress the need for a good estimate of the background for accurate filament mass measurements and we have shown that our approach allows us to decouple the filament contribution from the background with errors estimated around $\sim$15%–20% (dispersion of the residuals) in the case of features with moderate surface-brightness contrast.

We applied our method to the column density map calculated from *Herschel* observations of the Outer Galaxy in the Galactic longitude range of $l = 216.^\circ5$ to $l = 225.^\circ5$ (l217–224) to measure the filament properties and attempt to determine their role in the star formation process. We found that filaments are found at various distances between 0.5 and 7.5 kpc. They can be identified at various spatial scales, from lengths as short as $\sim$0.5 pc up to 30 pc and widths between 0.1 pc and 3 pc, most of which are typically resolved in the *Herschel* observations. The measured aspect ratios range between 3 and 30.

The column density PDF indicates that almost all the dense material with $N_{\rm H_2} \geqslant 6 \times 10^{21}\ {\rm cm}^{-2}$ is arranged into filamentary structure. However, not all high density material is associated with clumps *hosted* by the filamentary structure; a significant fraction are local density enhancements on the filaments hinting of a state of global collapse.

The majority of the clumps (74%) identified in previous studies are located within the borders of our filament sample. Nevertheless, we still found star formation going on *outside* the filaments. It is unlikely that these objects form in the filaments and are successively dispersed. However, we find a significant difference between the surface density of clumps on the filaments versus the ones outside, with the clumps on the filaments showing higher surface densities. Furthermore, we observe that the majority of the clumps outside the filamentary regions have surface densities below the value necessary for high-mass star formation (Krumholz & McKee 2008; Butler &

Tan 2012), hence it is very likely that they finally fragment into clusters of low-mass stars. This does not seem to be the case for the clumps on the filaments where the higher surface densities overcome the assumed threshold limit. It is worth noting that so far observation of regions with high-mass clumps have generally highlighted a larger filamentary structure in which they are embedded (Schneider et al. 2010; Hill et al. 2011; Peretto et al. 2013; Polychroni et al. 2013; Nguyen Luong et al. 2011). Hence, even if our data are not conclusive, the filamentary shape seems to be an important vehicle to channel enough material into small regions and to allow the formation of high-mass stars. Observations with higher spatial resolution toward the clumps outside our filament sample would determine if massive star formation also happens without filaments and, if that is the case, the relative number of those sources with respect to the number of massive clumps inside the filaments.

On the other hand, a significant number of filaments do not host any clumps. We estimated the mass per unit length, $M_{\rm line}$, for all the filaments in our sample and found that the structures without clumps all have a $M_{\rm line} \leqslant 16\ M_{\odot}\ {\rm pc}^{-1}$, which is the critical value for a filament sustained by the thermal pressure exerted by material with $T \sim 10$ K. Hence, these filaments are transient structures that are kept together by external pressure from the interstellar medium. The filaments hosting clumps, instead, span a large range of $M_{\rm line}$, between 1 and 100 $M_{\odot}\ {\rm pc}^{-1}$. Such a result is puzzling because, if the clumps are a direct result of filament collapse and fragmentation due to gravity, we would not expect to find clumps on any filament with $M_{\rm line} \leqslant 16\ M_{\odot}\ {\rm pc}^{-1}$. Any non-thermal contribution, which was not accounted for by our analysis, would increase the value of the $M_{\rm line,crit}$ and thus the number of filaments with no clumps. Such results agree with what is found for a few IRDCs in the inner Galaxy. Moreover, we found that the supercritical filaments $M_{\rm line} \sim 80$–$90\ M_{\odot}\ {\rm pc}^{-1}$ have more material aggregated in clumps, also hosting the most massive ones.

Thus, we suggest a possible scenario for fast formation of the filaments, where these structures and the initial seed for the clumps are formed at the same time. In such a scenario the global structure can be in equilibrium (or close to it), and the clump formation starts on local scales, induced by processes like flows or external pressures that locally enhance the linear density. We studied the local scales in the filament by analyzing the branches in which the filament can be divided. We confirmed that the branch $M_{\rm line}$ values are typically higher than those of the whole structure. This result is also in agreement with the protostellar objects found only on the supercritical filaments. Structures are created with a range of masses depending on the amount of surrounding material. In the most dense cases a mini-"starburst" process starts with a higher star-formation rate that can form protostellar objects very quickly. This scenario effectively decouples the clump formation from the filament evolution (at least in their early stages).

However, when we compare the $M_{\rm line}$ of the local substructures, we found a statistically significant difference between the filamentary subregions hosting prestellar clumps versus the ones with protostellar clumps. In particular, we found higher values of linear density in the subregions with protostellar clumps with respect to the ones with only prestellar clumps. While these results are still consistent with the fast formation scenario, it suggests that the differentiation might be set by the evolution of the structure. Filaments, after their formation, increase their $M_{\rm line}$ and progress to form prestellar clumps that evolve into protostars on timescales faster than the filament evolution. It is unlikely that the enhancement of the $M_{\rm line}$ is caused by the shrinking of the filament due to self-gravity, but our results play in favor of an accretion of material from the surrounding (within the filament itself or from the environment). Our data requires a moderate increase of linear density with time $\sim 10^{-4}\ M_{\odot}\ {\rm pc}^{-1}\ {\rm yr}^{-1}$, a rate compatible with the one measured for filaments in nearby molecular clouds.

Following Arzoumanian et al. (2013) we expect that all the filaments with widths larger than the Jeans length should be in a state of global collapse due to their gravity, since the internal thermal pressure alone is not able to sustain the structure. For the mean width of our filament sample of 0.5 pc, we expect that all structures with a central column density higher than $\sim 1.8 \times 10^{21}\ {\rm cm}^{-2}$ would be in dynamical collapse. However, since we do not measure any shrinking of the filament, we expect an increase of non-thermal support for those more condensed filaments. If such a result is really hinting at filaments in a state of global collapse, we do expect a larger number of those with respect to the one identified for the studies of nearby clouds Arzoumanian et al. (2013). This result requires additional confirmation for future molecular spectroscopic observations.

The authors are grateful to the anonymous referee for the useful comments that improved the presentation of the work. E.S. acknowledges support from the NASA Astrophysics Data Analysis Program grant NNX12AE18G. K.L.J.R. is supported by an Italian Space Agency (ASI) fellowship under contract number I/005/11/0. G.B. is supported by the Spanish MICINN grant AYA2011-30228-C03 (co-funded with FEDER funds). D.P. is funded through the Operational Program "Education and Lifelong Learning," which is co-financed by the European Union (European Social Fund) and Greek national funds. S.C.O.G. acknowledges support from the Deutsche Forschungsgemeinschaft via SFB 881 "The Milk Way System" (sub-projects B1 and B2). The authors are also grateful to M. Pereira-Santaella and N. Marchili for helpful suggestions.

E.S. is very grateful to Antonia Pierni and wishes to thank her for all the moments, dark and bright, they spent together while he was working on this research.

REFERENCES

André, P., Men'shchikov, A., Bontemps, S., et al. 2010, A&A, 518, L102
Aragón-Calvo, M. A., Jones, B. J. T., van de Weygaert, R., & van der Hulst, J. M. 2007, A&A, 474, 315
Arzoumanian, D., André, P., Didelon, P., et al. 2011, A&A, 529, L6
Arzoumanian, D., André, P., Peretto, N., & Könyves, V. 2013, A&A, 553, A119
Bond, N. A., Strauss, M. A., & Cen, R. 2010, MNRAS, 409, 156
Busquet, G., Zhang, Q., Palau, A., et al. 2013, ApJL, 764, L26
Butler, M. J., & Tan, J. C. 2012, ApJ, 754, 5
Canny, J. 1986, ITPAM, 8, 679
Compiègne, M., Flagey, N., Noriega-Crespo, A., et al. 2010, ApJL, 724, L44
Cormen, T. H., Leiserson, C. E., Rivest, R. L., & Stein, C. 2009, Introduction to Algorithms (3rd ed.; Cambridge, MA: MIT Press)
Csengeri, T., Bontemps, S., Schneider, N., et al. 2011, ApJL, 740, L5
Elia, D., Molinari, S., Fukui, Y., et al. 2013, ApJ, 772, 45
Elia, D., Molinari, S., Schisano, E., et al. 2010, A&A, 518, L97
Enoch, M. L., Evans, N. J., II., Sargent, A. I., et al. 2008, ApJ, 684, 1240
Fiege, J. D., & Pudritz, R. E. 2000, MNRAS, 311, 85
Galván-Madrid, R., Vázquez-Semadeni, E., Kim, J., & Ballesteros-Paredes, J. 2007, ApJ, 670, 480
Gomez, G. C., & Vazquez-Semadeni, E. 2014, arXiv:1308.6298
Gong, H., & Ostriker, E. C. 2011, ApJ, 729, 120
Gonzalez, R., & Woods, R. 1992, Digital Image Processing (Reading, MA: Addison-Wesley)
Gonzalez, R. C., & Woods, R. E. 2002, Digital Image Processing (Upper Saddle River, NJ: Prentice Hall)
Hacar, A., Tafalla, M., Kauffmann, J., & Kovacs, A. 2013, A&A, 554, A55
Hartmann, L. 2002, ApJ, 578, 914

Hartmann, L., & Burkert, A. 2007, ApJ, 654, 988
Hatchell, J., Richer, J. S., Fuller, G. A., et al. 2005, A&A, 440, 151
Heitsch, F., Ballesteros-Paredes, J., & Hartmann, L. 2009, ApJ, 704, 1735
Heitsch, F., & Hartmann, L. 2008, ApJ, 689, 290
Hennemann, M., Motte, F., Schneider, N., et al. 2012, A&A, 543, L3
Henning, T., Linz, H., Krause, O., et al. 2010, A&A, 518, L95
Hernandez, A. K., & Tan, J. C. 2011, ApJ, 730, 44
Hernandez, A. K., Tan, J. C., Kainulainen, J., et al. 2012, ApJL, 756, L13
Hildebrand, R. H. 1983, QJRAS, 24, 267
Hill, T., Motte, F., Didelon, P., et al. 2011, A&A, 533, A94
Inutsuka, S.-I., & Miyama, S. M. 1992, ApJ, 388, 392
Jackson, J. M., Finn, S. C., Chambers, E. T., Rathborne, J. M., & Simon, R. 2010, ApJL, 719, L185
Jiménez-Serra, I., Caselli, P., Tan, J. C., et al. 2010, MNRAS, 406, 187
Kainulainen, J., Beuther, H., Henning, T., & Plume, R. 2009, A&A, 508, L35
Kirk, H., Myers, P. C., Bourke, T. L., et al. 2013, ApJ, 766, 115
Krumholz, M., & McKee, C. F. 2008, Natur, 451, 1082
Larson, R. B. 1985, MNRAS, 214, 379
Molinari, S., Pezzuto, S., Cesaroni, R., et al. 2008, A&A, 481, 345
Molinari, S., Schisano, E., Faustini, F., et al. 2011, A&A, 530, A133
Molinari, S., Swinyard, B., Bally, J., et al. 2010a, A&A, 518, L100
Molinari, S., Swinyard, B., Bally, J., et al. 2010b, PASP, 122, 314
Motte, F., Bontemps, S., Schilke, P., et al. 2007, A&A, 476, 1243
Myers, P. C. 2009, ApJ, 700, 1609
Nguyen Luong, Q., Motte, F., Hennemann, M., et al. 2011, A&A, 535, A76
Novikov, D., Colombi, S., & Doré, O. 2006, MNRAS, 366, 1201
Ostriker, J. 1964, ApJ, 140, 1056
Padoan, P., Nordlund, Å., Kritsuk, A. G., Norman, M. L., & Li, P. S. 2007, ApJ, 661, 972
Palmeirim, P., André, P., Kirk, J., et al. 2013, A&A, 550, A38
Passot, T., & Vázquez-Semadeni, E. 1998, PhRvE, 58, 4501
Peretto, N., André, P., Könyves, V., et al. 2012, A&A, 541, A63
Peretto, N., Fuller, G. A., Duarte-Cabral, A., et al. 2013, A&A, 555, A112
Pilbratt, G., Riedinger, J. R., Passvogel, T., et al. 2010, A&A, 518, L1
Polychroni, D., Schisano, E., Elia, D., et al. 2013, ApJL, 777, L33
Qu, M., Shih, F. Y., Jing, J., & Wang, H. 2005, SoPh, 228, 119
Rathborne, J. M., Jackson, J. M., & Simon, R. 2006, ApJ, 641, 389
Rosolowsky, E., Dunham, M. K., Ginsburg, A., et al. 2010, ApJS, 188, 123
Ruprecht, J. 1966, BAICz, 17, 33
Rygl, K. L. J., Wyrowski, F., Schuller, F., & Menten, K. M. 2010, A&A, 515, A42
Schneider, N., Csengeri, T., Bontemps, S., et al. 2010, A&A, 520, A49
Sheth, J. V., Sahni, V., Shandarin, S. F., & Sathyaprakash, B. S. 2003, MNRAS, 343, 22
Sousbie, T. 2011, MNRAS, 414, 350
Tan, J. C. 2000, ApJ, 536, 173
Toalá, J. A., Vázquez-Semadeni, E., & Gómez, G. C. 2012, ApJ, 744, 190
Vázquez-Semadeni, E., Banerjee, R., Gómez, G. C., et al. 2011, MNRAS, 414, 2511
Vázquez-Semadeni, E., & García, N. 2001, ApJ, 557, 727
Ward-Thompson, D., André, P., Crutcher, R., et al. 2007, in Protostars and Planets V, ed. B. Reipurth, D. Jewitt, & K. Keil (Tucson, AZ: Univ. Arizona Press), 33